

**Baby Giants:
Finding Intermediate Mass
Black Holes in the Local Universe**

by

Hannah Sugarman
Class of 2009

A thesis submitted to the
faculty of Wesleyan University
in partial fulfillment of the requirements for the
Degree of Bachelor of Arts
with Departmental Honors in Astronomy

There is a theory which states that if ever anybody discovers exactly what the Universe is for and why it is here, it will instantly disappear and be replaced by something even more bizarre and inexplicable. There is another theory which states that this has already happened.

—DOUGLAS ADAMS

The Hitchhiker's Guide to the Galaxy

Acknowledgements

I simply would not be who I am today without the support of all of you. I have been blessed with many amazing friends and teachers in my life, all of whom have influenced me in countless ways. Quite simply, there are more people I'd like to thank than could fit in this entire thesis, and I apologize to all of you who have helped me along my way whose names I don't have room to include here.

The Wesleyan and Head-Royce communities have meant the world to me, and I thank all of you who have contributed to my education, or given me the support to get through it.

To my family, who fostered an inquisitive outlook on life, supported my whims and fancies, and have always offered the most sage advice. I love you, and would not be where I am today without you.

To Ed Moran, without whom none of this would have been possible. You always had confidence that I would pull it off, and you never let me doubt myself. Your support and guidance has been invaluable.

To Darik, Sam, and Karlen, for all the cooperation with the science of this project, and for all the laughs and good times along the way. Extra thanks to Darik for the BPT diagrams.

To Roy, for his everlasting patience and bottomless technical knowledge.

Finally, to Matt, for letting me teach you about AGNs, and for always being there to share the good times and the bad. Your influence has made me a better scientist, and the past four years would not have been the same without you by my side.

Contents

1	Introduction	1
1.1	The Importance of Intermediate Mass Black Holes	2
1.2	Finding IMBHs in The Local Universe	5
2	Building a Volume-Limited Sample	8
2.1	Defining Our Volume	9
2.2	The Sloan Digital Sky Survey	10
2.3	The Arecibo Legacy Fast ALFA Survey	11
2.4	The NASA/IPAC Extragalactic Database	12
3	Galaxy Distances and Luminosities	14
3.1	Determining Distance	14
3.2	Photometry and Absolute Magnitudes	19
3.3	Absolute Magnitudes	24
3.4	Spatial Distribution of the Galaxies	26
3.5	Absolute Magnitude Distribution	27
3.6	Sample Completeness	27
4	Spectroscopy	32
4.1	Spectral Signatures of AGNs	32

4.2	Physical Explanation of AGNs	37
4.3	Obtaining the Spectra	38
4.4	Starlight Subtraction	40
4.5	Results from Spectroscopy	42
4.6	Completeness of SDSS	60
5	Summary and Conclusions	63
A	Distance Calculations	65
B	Spectral Absorption and Emission	67
C	The Nature of LINERs	71
	Bibliography	76

Chapter 1

Introduction

Black holes are some of the most fascinating objects in our universe. For over a century they have captivated the imaginations of millions and have become one of the few scientific objects that are household names. In science fiction, black holes fuel spacecraft, provide pathways to other universes, and slow down time. Artists and musicians use black holes as metaphors for dark emotional states. We call the piles of paper on our desks or junk in our dressers “black holes” where our possessions and time get lost. There was even a conspiracy theory that the Large Hadron Collider would create a mini-black hole and destroy the Earth. Clearly, black holes have the power to mystify and intrigue us.

Scientifically, black holes are just as fascinating. Although the basic physics describing the nature of black holes is well established, there is much that is still unknown about the formation of BHs and how they interact with their environment. The goal of this research is to help refine our understanding of how black holes evolve.

The black holes that we observe in the universe fall into two different categories: stellar-mass and supermassive black holes. Stellar-mass black holes are formed from the gravitational collapse of a single massive star, and range in mass from $\sim 1.5 - 3M_{\odot}$ (Bombaci 1996) to $\sim 33M_{\odot}$ (Prestwich et al. 2007). Supermassive BHs are found in the centers of galaxies, and range in mass from $\sim 10^6 M_{\odot}$ to

$\sim 10^9 M_\odot$. It is now widely accepted that supermassive black holes exist at the center of most, if not all, massive galaxies (e.g., Kormendy & Richstone 1995; Ho 2008). However, there is much doubt surrounding how these supermassive BHs form. Finding intermediate-mass black holes to fill in the gap between stellar-mass and supermassive BHs will help us understand the formation of galaxies and the role of black holes in galactic evolution.

1.1 The Importance of Intermediate Mass Black Holes

Observations have revealed some close connections between supermassive black holes and their host galaxies. There is strong evidence that the mass of a galaxy's central black hole (M_{BH}) is directly related to σ , the velocity dispersion of the stars in the galactic bulge (e.g., Gebhardt et al. 2000; Tremaine et al. 2002, see Fig. 1.1). Connections have also been found between M_{BH} and bulge mass (M_{bulge}) (Kormendy & Richstone 1995; Marconi & Hunt 2003, see Fig. 1.2), and between M_{BH} and bulge luminosity (L_{bulge}) (Bentz et al. 2009, see Fig. 1.3).

Initially, these correlations may not seem surprising given the massiveness of black holes, but in reality the direct “sphere of influence” of a supermassive black hole is quite small in comparison to the size of the entire galaxy, or even its bulge. This means that it is impossible for the black hole to directly influence the properties of the host galaxy on such a large scale, so the observed correlations must indicate a more complex connection between nuclear black holes and global galactic properties. Additionally, black holes are predominantly found in massive, bulge-dominated galaxies, indicating that the formation of BHs and bulges may be related. Together, all of these clues indicate that black holes are closely tied to

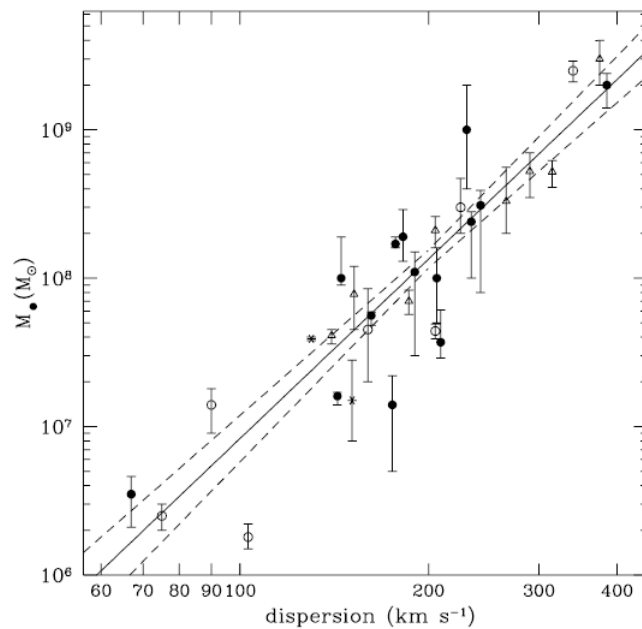


Figure 1.1: The $M_{BH} - \sigma$ relationship (from Tremaine et al. 2002).

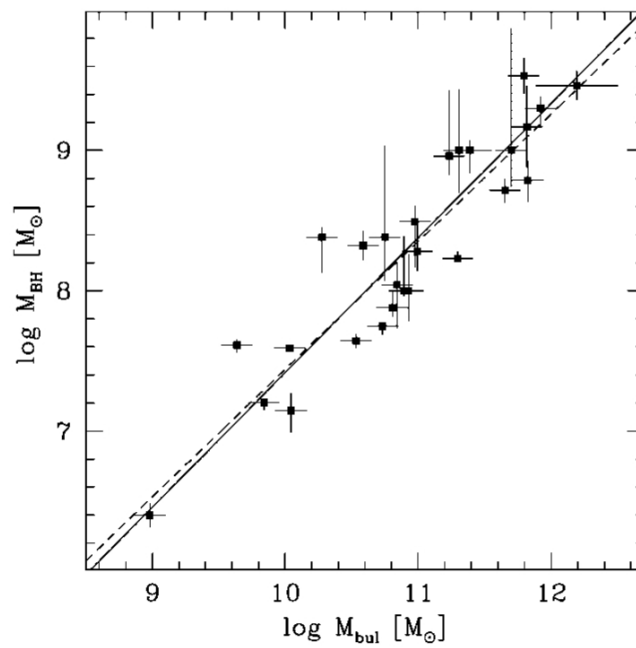


Figure 1.2: The $M_{BH} - M_{bulge}$ relationship (from Marconi & Hunt 2003)

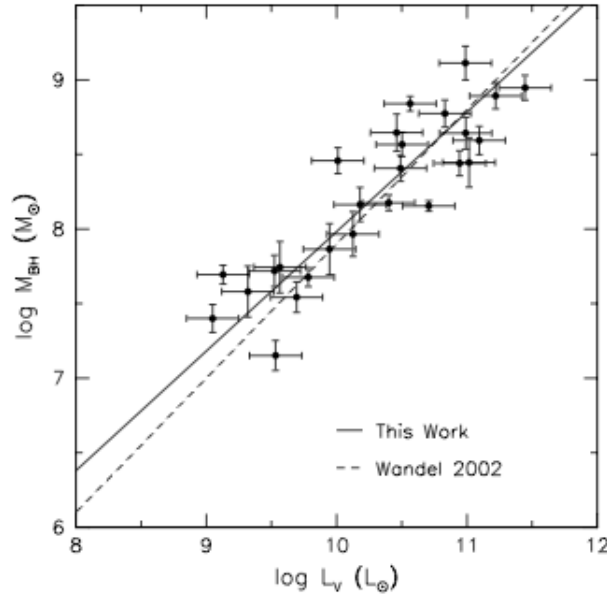


Figure 1.3: The $M_{BH} - L_{bulge}$ relationship (from Bentz et al. 2009).

their host galaxies, most likely through a common formation history. The hierarchical merging model of galaxy formation could explain these close connections. The premise of the hierarchical merging model is that the large galaxies that we observe today were created by smaller progenitor galaxies merging over time. By adopting the premise of hierarchical merging as the most likely vehicle for galaxy formation, we can begin to untangle how black holes evolved in conjunction with their host galaxies. Our eventual goal is to understand how supermassive black holes came to be.

Intermediate-mass black holes (IMBHs), with masses of $10^3 - 10^6 M_{\odot}$ span the gap between stellar-mass and supermassive BHs. These IMBHs are likely to be found in small, low-luminosity galaxies, based on extrapolation from the $M_{BH} - M_{bulge}$ and $M_{BH} - L_{bulge}$ relationships discussed above (Figs. 1.2, 1.3). Indeed, the two smallest supermassive BHs that have been detected, NGC 4395 ($M_{BH} \approx [3.6 \pm 1.1] \times 10^5 M_{\odot}$, Peterson et al. 2005) and POX 52 ($M_{BH} \approx$

$1.6 \times 10^5 M_{\odot}$; Barth et al. 2004) have been found in low-luminosity galaxies.

Hierarchical galaxy formation models imply that observing IMBHs and their host galaxies could give us much information about galaxy formation. These small dwarf galaxies allow us to essentially look back in time, down the galactic “food chain” to see what the ancestors of large galaxies probably looked like. Therefore, the distribution and properties of IMBHs and their host galaxies could provide powerful constraints on our models of galaxy and black hole formation.

1.2 Finding IMBHs in The Local Universe

Not surprisingly, black holes cannot be directly observed. Evidence for supermassive black holes, by necessity, must come from observing the effects that a black hole exerts on its environment. In the case of bright, nearby galaxies, it is possible to detect the presence of a central supermassive BH from the gravitational effects that the BH has on stars in its vicinity. If the nucleus of the galaxy can be resolved, the velocity distribution of the stars in the nucleus can confirm the presence of a supermassive black hole. These observations have been done successfully for nearby, bright galaxies such as M31, M32, and NGC 3115 (Kormendy & Richstone 1995), as well as for the Milky Way (Ghez et al. 2005). However, in order to use direct dynamical measurements to detect black holes, one must be able to resolve the gravitational sphere of influence of the black hole. This is not possible for most galaxies, and would be especially difficult for the dwarf galaxies which are likely to host IMBHs, because the radius of the sphere of influence of the black hole is directly related to M_{BH} . With current imaging techniques, we would only be able to resolve the sphere of influence of an IMBH for extremely nearby galaxies. Clearly, this is a problem for IMBH studies, so

dynamical detection techniques are not appropriate. Therefore, another way of detecting black holes is necessary.

If a black hole is actively accreting matter, the energy released during this process leaves a tell-tale signature in the galaxy’s optical spectra (see Sec. 4.1 for details). In the standard model of an Active Galactic Nucleus (AGN), the central black hole is surrounded by a disk of accreting material which is heated to very high temperatures as its gravitational potential energy is released. This hot matter emits radiation in the X-ray and far UV regions of the continuum, and gives rise to signature emission lines in the optical spectrum of the nucleus (Ho 2008). Although there have been attempts to find AGNs using X-ray data, most AGN surveys rely on looking for the distinct AGN emission in the optical spectra of galaxies. It is important to remember that spectral surveys will not detect every black hole, but only those which are actively accreting at a fast enough rate for emission to be detected above the continuum level of the galaxy. However, due to the reliability of optical spectra as a means for identifying BHs (as opposed to X-ray surveys, which cannot determine whether an X-ray source is truly an AGN), and the fact that spectra can be easily obtained for many galaxies, spectral surveys are still the best way to find nuclear black holes.

There have been other surveys attempting to find IMBHs. Beginning in 1985, Ho, Filippenko, and Sargent (Filippenko & Sargent 1985; Ho et al. 1995, 1997a,b,c, 2003, hereafter HFS) conducted an optical spectroscopic survey searching for “dwarf” (low-luminosity) AGNs. However, their survey was based on the apparent magnitude of host galaxies, resulting in a significant bias towards luminous objects. This bias towards bright galaxies is exactly the opposite of what we hope for, since we expect to find IMBHs in low-luminosity and low-mass galaxies. Therefore, magnitude-limited samples will be inherently less successful at finding

IMBHs, and we must take a different approach. By constructing a volume-limited sample we can avoid observational bias towards bright galaxies.

Additionally, a complete volume-limited sample has the potential to give us two more factors that can constrain models of black hole formation. First, having a complete catalogue of local active galaxies would allow us to calculate the local mass function of active black holes (see Greene & Ho 2007b, for a discussion of the black hole mass function). Having an accurate BH mass function for the local universe would allow us to constrain models of theoretical black hole “seeds” formation, especially if we are able to compare a local mass function to a high-redshift mass function (Greene & Ho 2007b). Secondly, models of supermassive black hole evolution predict the black hole “occupation fraction” (i.e., the percent of galaxies with supermassive BHs), which depends on the initial parameters of the seed black holes (Volonteri et al. 2008). Therefore, having a more accurate measurement of the BH occupation fraction in the local universe could be a powerful tool for constraining the joint evolution of BHs and galaxies. Clearly, having a volume-limited sample will allow us to probe the properties of the local universe in a very meaningful way.

Eventually, we want to be able to conduct a survey over a large volume of space. However, it is first necessary to examine in detail the process of putting together a volume-limited sample, so that we have a solid understanding of how best to go about a volume-limited spectroscopic survey. Therefore, the process described in the following chapters serves as a pilot study for future work, which will take place on a much larger scale. We will discuss the creation of our sample in Chapter 2, and the distribution and luminosities of the sample in Chapter 3. The spectral analysis and results will be discussed in Chapter 4, as well as the implications that this research has for future surveys of IMBHs.

Chapter 2

Building a Volume-Limited Sample

Now that we have established the importance of obtaining a volume-limited sample, we must confront the details of how to accomplish this task. There are two main challenges to constructing a volume-limited sample: completeness and absence of bias. Additionally, any resource from which we draw our data must have redshift data so that we can establish distances to our objects prior to conducting any follow-up observations. There are three resources which best serve these purposes: the Sloan Digital Sky Survey (SDSS, Sloan), the Arecibo Legacy Fast ALFA Survey (ALFALFA), and the NASA/IPAC Extragalactic Database (NED). These choices are ideal because they cover a large area of the sky and include a significant fraction of the nearby population of galaxies.

Additionally, the combination of the three resources gives us access to a wide range of wavelength data that will help us achieve completeness. The SDSS is an optical survey, which should contain almost all nearby bright galaxies. ALFALFA is an HI survey, which detects the 21-cm emission created by a spin-flip transition of neutral hydrogen. Although this radiation is emitted infrequently by any single hydrogen atom, even very low-mass galaxies contain enough neutral hydrogen to emit a considerable amount of HI radiation. Therefore, low surface-brightness objects can be detected by their HI line, even though they might be missed in surveys at visual wavelengths. Because of this phenomenon, we include ALFALFA

data in order to increase our completeness at faint magnitudes. Detecting low surface brightness objects is an especially important aspect of our search for IMBHs, which are expected to reside in low-luminosity galaxies. Therefore, these two surveys should complement each other, with SDSS contributing luminous galaxies to our sample, and ALFALFA contributing at the low-luminosity end. Since NED contains all galaxies for which there is published data, it should serve as a back-up for any galaxies that slipped through the cracks in both SDSS and ALFALFA.

2.1 Defining Our Volume

We choose an area of the sky where SDSS and ALFALFA overlap: from $09^h36^m00^s$ to $13^h52^m00^s$ in right ascension and 10° to 16° in declination. This region is also chosen for convenience of spring follow-up observations. The size of the region was originally constrained by a relatively small area of overlap between SDSS and an early release of ALFALFA data, although both surveys have since released more data, increasing the total sky coverage. When the spring section of ALFALFA is complete (between $\alpha = 7^h30^m - 16^h30^m$ and $\delta = 0^\circ - 36^\circ$), it will lie almost entirely within the SDSS footprint, giving us an eventual overlap area of $\sim 4800 \text{ deg}^2$ (Giovanelli et al. 2005).

Unfortunately, the original region of overlap that we chose for our study includes the Virgo Cluster, a unique environment which could skew our results. Because this small sample is serving as a pilot study for later work over a larger area of the sky, we want to be able to generalize our results, and therefore we eliminate all possible Virgo Cluster objects from our sample. We adopt the coordinates $\alpha = 12^h30^m51^s$, $\delta = 12^\circ.4$ for the center of the Virgo cluster and a cluster radius of 10° , as given in Mould et al. (2000). This corresponds to eliminating

the range in RA from $11^h50^m00^s$ to $13^h12^m00^s$ across our entire 6° -wide declination strip. Our final sample area spans $\sim 260 \text{ deg}^2$, about 5% of the eventual ALFALFA-SDSS overlap region. The moderate size of this area enables us to obtain more completeness than would be possible with a larger sample, while still containing enough objects to make it a viable pilot study.

Based on analysis done by Dieck (2008) we adopt a redshift limit of $z \leq 0.0177$, corresponding to a distance of $\sim 80 \text{ Mpc}$ (after distance corrections, see section 3.1). This limit was chosen because a galaxy similar to NGC 4395 (the prototypical dwarf AGN) would be detected by ALFALFA if it were located at $z = 0.0177$ or closer, even if SDSS did not detect it (Dieck 2008). We do not impose any lower limit on z , because there is no reason at this time to omit objects with negative velocities. We will explore the appropriateness of this redshift limit in relation to the completeness of our sample in Section 3.6.

2.2 The Sloan Digital Sky Survey

Over more than eight years of observations, the Sloan Digital Sky Survey has established itself as the most extensive optical survey to date. The survey has obtained deep multicolor optical images covering more than a quarter of the sky ($11,663 \text{ deg}^2$), and has spectral data covering $9,380 \text{ deg}^2$. Sloan is currently on its seventh data release (DR7), which contains 1,640,960 individual spectra, including 929,555 that have been classified as galaxies (Abazajian et al. 2008).

The SDSS uses a dedicated, custom-designed 2.5 meter f/5 modified Ritchey-Chrétien telescope at Apache Point, New Mexico (York et al. 2000). The telescope is equipped with a 120-megapixel camera covering an area of 1.5 deg^2 , as well as a fiber-optic spectroscope capable of obtaining 640 spectra at a time. Specialized

software pipelines automatically analyze the data, perform photometry, select objects for spectroscopic observations, and subsequently reduce and analyze spectral data (York et al. 2000).

The results from these reduction pipelines are stored in databases that are publicly available through the Sloan website. Model-based magnitudes for all objects are given (see Sec. 3.2) as well as *fiberMag*, the flux over the three-arcsecond diameter of the spectroscopic fiber. Additionally, all objects for which spectra have been obtained have been reduced and analyzed and categorized as galaxies, stars, sky spectra, QSOs, or unknown objects. This reduction process includes subtraction of the background sky spectra and “cleaning” of cosmic-rays. All objects with spectra have a calculated redshift (z).

For our sample, we query the SDSS *SpecObj* table for all objects with spectra in our spatial and redshift range, except for those spectra identified by Sloan as sky or stellar spectra (*SpecClass* = 1, 5, or 6). However, this simple query returns many objects that we do not want in our sample. First, many large and bright galaxies have multiple spectral observations of their nucleus or extranuclear regions, so it was necessary to remove duplicate observations to avoid double-counting any galaxies. Additionally, our query accepted objects with unknown spectral type (*SpecClass* = 0), many of which were identified as stars using visual inspection of the image and spectra. After eliminating all multiple observations, stars, or otherwise non-galactic spectra, we have 319 SDSS galaxies in our region.

2.3 The Arecibo Legacy Fast ALFA Survey

When complete, ALFALFA will cover 7,074 deg² and will detect more than 25,000 extragalactic HI sources. ALFALFA maintains a public database populated

by periodic data releases, as well as a private database with data displayed as they become available. We have access to the private database, although since the recent release of Catalog 3 the data we use are publicly available.

In the same manner as we queried SDSS, we query ALFALFA for all galaxies within our volume range. ALFALFA contains 435 HI sources in our volume. Once we have these objects from ALFALFA, we cross-correlate this list against our previously identified objects from SDSS. After removing many duplicate objects, we have 312 ALFALFA-only objects. However, these will not all remain in our final sample, as many of them are optically invisible HI-only sources. We will discuss the culling of these objects in Section 3.3.

2.4 The NASA/IPAC Extragalactic Database

The largest catalog of all known galaxies is the NASA/IPAC Extragalactic Database¹ (NED). This catalog contains a list of extragalactic sources compiled from all published literature. NED contains positions, redshifts, and photometric data for galaxies, if this information is available in the literature. Additionally, NED provides bibliographic references for individual objects. As of March 2009, NED contained 163 million objects, although this number includes 154 million objects integrated into the database from SDSS DR6 (recall that our survey contains the more recent DR7 data).

There are several reasons why NED may contain objects that are excluded from SDSS. Sloan has magnitude limits on its spectral targets, so some very high surface-brightness galaxies might not have been selected as targets because the

¹This research has made use of the NASA/IPAC Extragalactic Database (NED) which is operated by the Jet Propulsion Laboratory, California Institute of Technology, under contract with the National Aeronautics and Space Administration.

spectra would saturate. (However, some high surface brightness galaxies have extranuclear spectra, and therefore are included in our 319 SDSS objects). Additionally, spectroscopic fibers can be placed no closer than 55 arcseconds apart when spectra are taken in Sloan. Therefore, close pairs of galaxies may only have a spectrum of one of the objects. There may also be NED objects that are cataloged from radio or X-ray surveys that are not included in Sloan.

As with Sloan and ALFALFA, we query the NED database for galaxies, galaxy pairs, and QSOs within our position and redshift limits. After removing duplicate objects from within NED results, NED contains 334 objects in our region, 21 of which are not included in SDSS or ALFALFA.

In total, we have 652 unique objects identified in this region of space. We are now prepared to begin examining the basic characteristics of these galaxies.

Chapter 3

Galaxy Distances and Luminosities

With the list of objects in our region now defined, we want to understand the characteristics of our sample prior to conducting a spectroscopic study. The SDSS, ALFALFA, and NED databases give us basic information about redshift and photometry, allowing us to calculate the distances to our objects, and subsequently their absolute magnitudes. The details of this process are discussed in this chapter.

3.1 Determining Distance

Although all of our objects have redshift data, calculating the distances to these objects is a more involved process than simply applying Hubble’s Law. All of these objects are in the local universe, which means that their radial velocities are small enough to be significantly impacted by local peculiar velocity effects that are not negligible with respect to the rate of cosmic expansion. Following the procedure adopted in NED, we use the method outlined in Karachentsev & Makarov (1996) for corrections to the rest-frame of the Local Group, and Mould et al. (2000) for further corrections to account for the gravinometric effects of the Virgo cluster and the Great Attractor. By accounting for infall toward these massive structures, the process outlined below converts observed heliocentric velocities to velocities that reflect expansion of the universe (see Appendix A for a step-by-step explanation

of the process). This corrected velocity may then be used in Hubble's Law for distance estimations.

Local Group Velocity

The most fundamental problem with using heliocentric velocities to measure distance is the effect of the Sun's own peculiar motion within the Milky Way. With respect to local stars, the sun has a peculiar velocity of 16 km s^{-1} in the direction of $(l = 53^\circ, b = 25^\circ)$ within the Galaxy, in addition to the rotation around the center of the Galaxy of $220 \pm 15 \text{ km s}^{-1}$ ($l = 90^\circ, b = 0^\circ$) with respect to the local standard of rest (Karachentsev & Makarov 1996). Correcting for these motions gives the observed galaxy's velocity with respect to the Galactic center.

Additionally, the gravitational pull of the Local Group imparts another peculiar velocity to the Galactic center, which is falling towards the center of the Local Group with a velocity of about 100 km s^{-1} in the direction of M31. These effects can all be encompassed by a single equation that transforms an object's heliocentric velocity into a velocity with respect to the center of the Local Group, based only on the object's Galactic coordinates (l, b) and heliocentric velocity, V_H :

$$V_{LG} = V_H + V_a(\cos(b) \cos(b_a) \cos(l - l_a) + \sin(b) \sin(b_a)) \quad (3.1)$$

where $V_a = 316 \text{ km s}^{-1}$, $b_a = -4^\circ$, and $l_a = 93^\circ$. These represent the velocity and direction of the sun's motion with respect to the center of the Local Group. This equation encompasses both the effects of solar motion and of the entire Galaxy's motion with respect to the Local Group (Karachentsev & Makarov 1996).

Final Velocity Corrections

The correction from heliocentric velocity to the Local Group velocity is crucial, but the Local Group itself is moving with respect to the rest frame of the Cosmic Microwave Background (CMB). The most accurate way to correct for this, especially for objects at small redshifts, is to consider these velocity perturbations with respect to large-scale gravitational attractors. Mould et al. (2000) have developed a linear multiattractor model that we use to correct Local Group velocities for infall into the Virgo Cluster and the Great Attractor. This model calculates the component of a galaxy's radial velocity (with respect to the Local Group) induced by an attractor:

$$V_{infall} = V_{fid} \cos \theta + V_{fid} \left(\frac{V_{LG} - V_a \cos \theta}{r_{oa}} \right) \left(\frac{r_{oa}}{V_a} \right)^{1-\gamma} \quad (3.2)$$

where V_{fid} is a constant representing the infall velocity towards that attractor at the Local Group, r_{oa} is the distance between the attractor and the object (expressed as a velocity), and V_a and γ are constants peculiar to individual attractors (see App. A for values for the Virgo Cluster and the Great Attractor). We apply this model to the Local Group velocity for all of our objects, first correcting them for infall into the Virgo Cluster, and subsequently for infall into the Great Attractor. The correction due to the Shapely Supercluster is insignificant for our objects, so we chose to omit it. With this final corrected velocity, Hubble's law can be applied to obtain distances to our objects. Following NED, we adopt a value of $73 \text{ km s}^{-1} \text{ Mpc}^{-1}$ for Hubble's constant.

Note that, in general, we would want to exclude objects that may be members of the Virgo Cluster before applying these corrections. In our case, we have already

excluded Virgo Cluster members, so this is not necessary, but in larger samples, Virgo cluster objects would need to be considered separately from the rest of the sample.

As a final note, these corrections are less accurate for the closest galaxies. Nearby galaxies have an inherently smaller recessional velocity, so peculiar velocities due to gravitational interactions can constitute a larger fraction of their total velocity. Therefore, objects of interest with a small heliocentric velocity ($V_H < 600 \text{ km s}^{-1}$) should be examined on a case-by-case basis.

Results

As can be seen in Figure 3.1, the corrections from pure heliocentric velocities to corrected velocities makes a significant and systematic difference in our final distance calculations for our sample galaxies. Due to the proximity of the Virgo Cluster ($D \approx 14 \text{ Mpc}$), our corrected values generally result in systematically larger cosmic velocities, and therefore greater distances than pure heliocentric velocities. This effect is caused by the large gravitational attractors effectively “slowing down” the cosmic velocities of these objects.

However, for very close objects, the reverse effect occurs, because those galaxies are moving away from us as they “fall into” the Virgo Cluster, and when that effect is removed their corrected cosmic velocity is slower.

There are also a number of objects for which distances have been measured using observational methods such as Cepheid variable stars, Type Ia supernovae, or the Tully-Fisher relation. These calculated distances are available in the “NED-0.5D” database on the NED website. There are 36 galaxies in our sample for which distances are available in this database. The comparison between our dis-

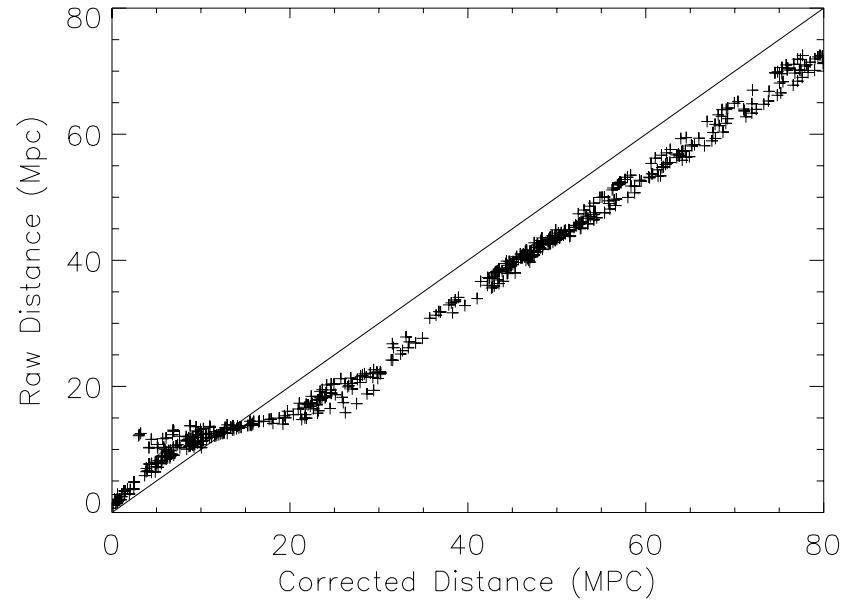


Figure 3.1: Comparison of infall-corrected distances to raw distances based only on heliocentric velocity. The solid line is the identity, $y=x$.

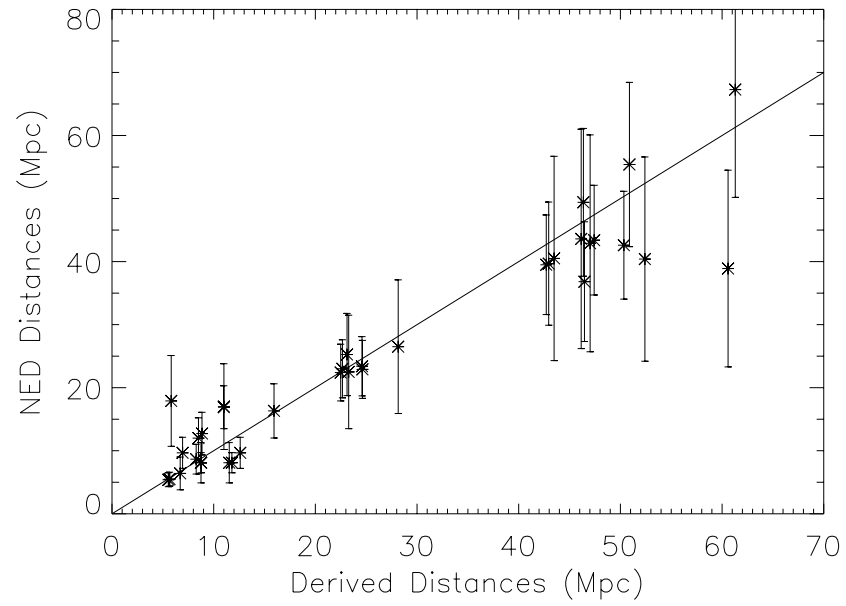


Figure 3.2: Distances from the NED-0.5D database versus our derived distance values. The solid line is the identity, $y=x$.

tance calculations and the observationally measured distances (from NED) can be seen in Figure 3.2. Although there is a fair amount of scatter, it is comparable to the error in the published measurements. Significantly, our values correspond well to the NED values even at very close distances, where we expect our error to be greatest. Therefore we have confidence that our distance calculations are sufficiently accurate over the full range of heliocentric velocity of our sample objects.

3.2 Photometry and Absolute Magnitudes

Now that we have distances to our objects, we want to obtain estimates of their luminosities. We use SDSS photometry for this purpose (remember that all of our objects, even those that are only catalogued with redshifts in ALFALFA, are in the SDSS footprint and therefore have SDSS images and photometry). We use the SDSS *g*-band for our photometry, which is similar to the Johnson *B*-band.

The SDSS databases provide two different options for photometric calculations. First, they offer the calculated Petrosian magnitude (*petroMag*), calculated by measuring all the flux within a circular radius defined by the extent of the azimuthally averaged light profile. Specifically, SDSS adopts the algorithms from Blanton et al. (2001) and Yasuda et al. (2001) to define the Petrosian radius and Petrosian flux. Additionally, SDSS also fits two different surface brightness models to the image of each galaxy in each band: a pure deVaucouleurs profile (Eq. 3.3) and a pure exponential profile (Eq. 3.4):

$$l(r) = l_0 \exp \left(-7.67 \left(\frac{r}{r_e} \right)^{1/4} \right) \quad (3.3)$$

$$l(r) = l_0 \exp \left(-1.68 \left(\frac{r}{r_e} \right) \right) \quad (3.4)$$

SDSS automatically determines which of these models provides a better fit for each individual object, and returns that value as *modelMag*. However, for each galaxy, the SDSS pipelines return many different values for both *petroMag* and *modelMag*, each associated with a different “photometric point” (see Fig. 3.3). Because the two different models and the calculation of the Petrosian radius are all dependent on the precise details of the surface brightness profile of a galaxy, neighboring photometric points can return values that can be up to 7 or 8 magnitudes apart. This complication must be addressed before we can adopt photometric values for our objects.

Choosing our Photometric Points

In most cases there are several points for each galaxy where the SDSS system has calculated photometry. Additionally, in many of our objects there is no clear galactic nucleus on which to center the photometry (see Fig. 3.3). For consistency, we choose to use the photometric point with the brightest calculated magnitude, because we are interested in the maximum amount of integrated light from the galaxy. In order to obtain this value we use an iterative process that searches within 15 arcseconds of the galaxy’s “central” coordinates and returns the minimum value for apparent magnitude.

In addition, we queried SDSS directly for the magnitude of the photometric point closest to the RA and Dec of the nucleus of the galaxy, if present, or spatial center of the galaxy, in the case of no obvious nucleus. When the brightest point differed greatly from the nuclear photometry, individual inspection was used to handle galaxies whose photometry was contaminated by a separate source (see

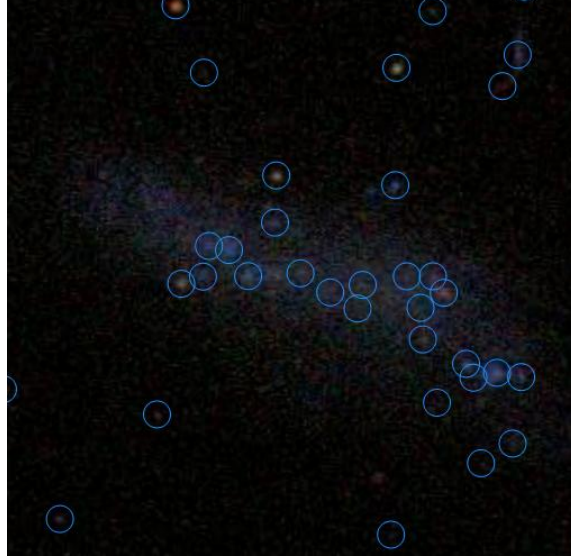


Figure 3.3: This galaxy illustrates the potential difficulty in determining the proper photometric point to use. There is no clear nucleus, and there are many separate photometric measurements.

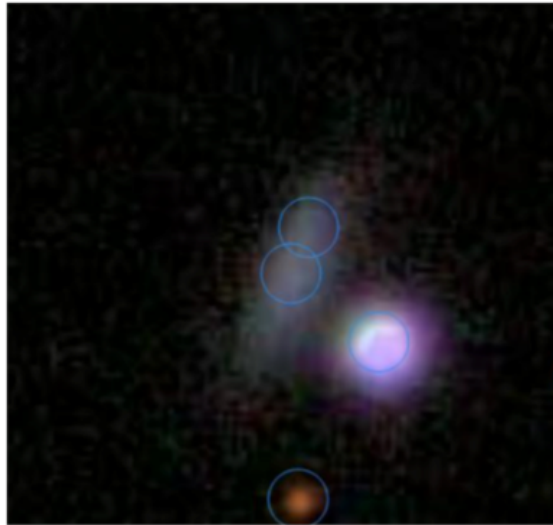


Figure 3.4: The algorithms for brightest magnitude would fail in this case. The galaxy of interest is on the left, but the photometry for a bright foreground star would return the brightest magnitude. Individual inspection would yield a more accurate choice for the photometric point to use for this object, although some contamination might be unavoidable.

Fig. 3.4). However, there are cases, including the galaxy in Figure 3.4, where contamination from another source may be present or unavoidable, potentially introducing a source of error into our measurements.

ALFALFA-only Objects

For ALFALFA-only objects, the same basic method for photometry applies. However, in cases where there is no ALFALFA-determined optical counterpart, the central positions as given by ALFALFA could potentially be quite different from the position of any optical counterpart that may be present. This is due to the fact that ALFALFA is a drift-scan survey with a relatively large beam, resulting in poor position resolution. Therefore, we adopt a much larger search radius (75 arcsec, based on analysis done by Dieck 2008) in order to include any possible source of the HI radiation. At this point, this is the only concession made to ALFALFA-only objects. Further refinement of which objects will be included in our final sample is discussed in Section 3.3.

Type of Photometry

Now that we have a way to resolve the issue of multiple photometric points, and a way to include ALFALFA objects, we need to choose which type of magnitude (*petroMag* or *modelMag*) to adopt for the photometric calculations. Because the Petrosian magnitude is more consistent, and is fundamentally based on simple photometric techniques, we chose to use it over than the model magnitude in almost all cases. However, there are some cases where the Petrosian magnitude returned a significantly different value than the model magnitude (off by more than one standard deviation, see Fig. ??). For instance, sometimes a Petrosian

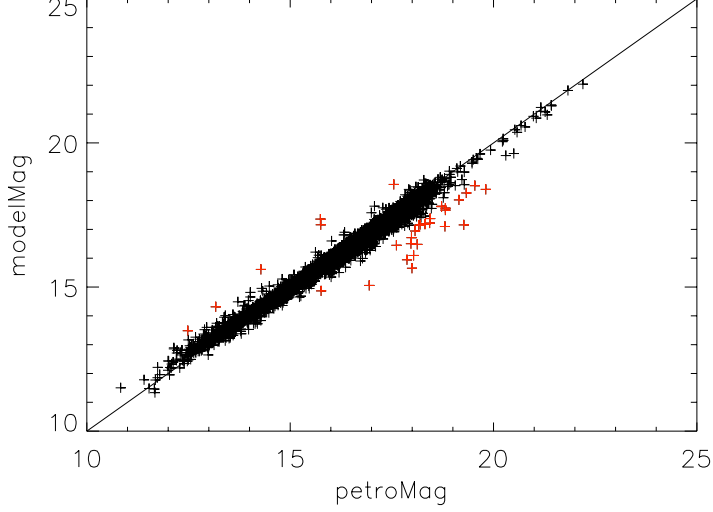


Figure 3.5: Distribution of *modelMag* versus *petroMag* for the sample. Objects where the offset from the identity line differs by more than one standard deviation ($\sigma \approx 0.15$) are shown in red.

radius is adopted that is inappropriately small, but the *modelMag* appears to be accurate for the object. We inspected these objects by hand to determine if errors had occurred in the SDSS pipeline and which magnitude should be adopted.

Although this process results in fairly accurate measurements of photometry for our objects, it should be noted that the SDSS photometric pipelines have inherent limitations, and tend to underestimate the Petrosian radius and model magnitude, resulting in magnitudes that are sometimes fainter than they should be. Therefore, this is only a preliminary photometric step, and once AGNs are found, it is important to re-evaluate the validity of their SDSS photometry.

With our photometry in hand, and the distances to our objects determined, we can now apply the distance modulus (Eqn. 3.5) to get the absolute magnitudes

of objects in our sample.

$$g - M_g = 5 \log(d/10\text{pc}) \quad (3.5)$$

3.3 Absolute Magnitudes

Figure 3.6 shows the preliminary absolute magnitude distribution for all galaxies in the sample thus far. Because it is not practically possible to form a complete sample over all magnitudes, we must establish an absolute magnitude cut-off, and exclude all objects dimmer than our limit. We chose to limit our sample to objects with an absolute magnitude brighter than -14 , where we believe we can maximize our completeness. Objects with $M_g \leq -14$ should be detectable at the far end of our distance range, while fainter objects may be missed. This is a conservative estimate, in order to obtain as much completeness as possible. The appropriateness of this absolute magnitude cut will be discussed in Section 3.6. Additionally, many of the objects fainter than -14 are questionable ALFALFA detections that we do not want in our final sample (see below). Simply applying this cut to our sample, we eliminate 10 NED objects, 49 SDSS objects and 215 ALFALFA-only objects. Because of the systematic errors in the SDSS pipelines, we individually inspect the 59 faint SDSS and NED objects to ensure that they are not being incorrectly culled. No objects were re-introduced into our sample after individual inspection.

Culling the ALFALFA-only objects

Unlike the objects in SDSS and NED, it is still uncertain whether all ALFALFA objects remaining in the sample are actually galaxies within our velocity range

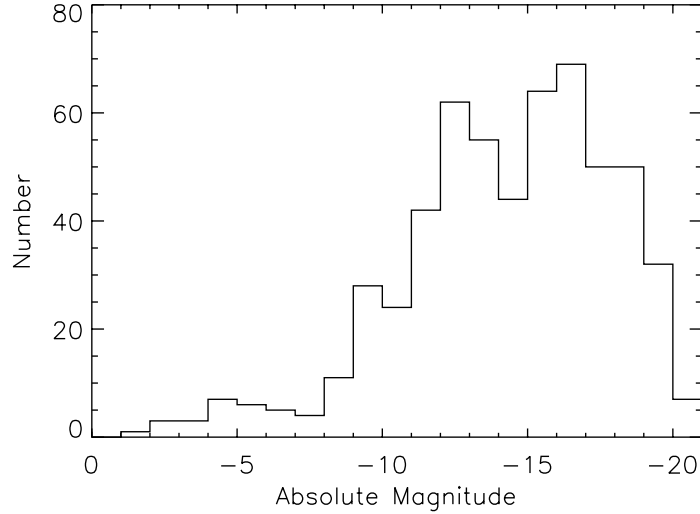


Figure 3.6: The distribution of calculated absolute magnitudes for our original sample.

and absolute magnitude limit. There are a number of factors contributing to the legitimacy of ALFALFA detections.

Because HI emission can often be diffuse, calculating a central position is not necessarily straightforward. First, ALFALFA provides the ellipse center, which is the center of a forced elliptical isophotal fit at half of the peak power level (Giovanelli et al. 2007). Secondly, a centroid position is given, derived from a map of the total HI emission within 100 arcmin^2 . Finally, if an optical counterpart to the HI emission has been identified by the ALFALFA team, the position of the optical center is given. We eliminate objects where the ellipse center and centroid positions are more than 75 arcseconds apart. These objects would introduce a great deal of uncertainty to our sample, and are likely to be faint and diffuse, possibly Galactic, sources.

The remaining objects fall into three categories: (1) Objects with optical counterparts identified by ALFALFA; (2) Objects with a possible optical counterpart

that can be confidently identified by eye in SDSS images but do not have spectra; (3) Objects with no clear optical counterpart within 1 arcmin. Objects in category (3) initially appeared to meet our absolute magnitude criteria because there is some other object in the same field, usually a foreground star or bright background galaxy, that is not the optical counterpart but has photometry that was returned in our searches.

Of these three types of objects, we keep all objects in categories (1) and (2), while rejecting category (3) objects as HI-only. Any potential optical counterpart to these sources would be too faint to fulfill our absolute magnitude criterion. A total of 35 ALFALFA-only objects remain in our sample. Adding these to our 270 galaxies drawn from the SDSS and 11 NED-only objects, we have a total of 316 galaxies in our sample.

3.4 Spatial Distribution of the Galaxies

Figures 3.7 and 3.8 illustrate the spatial distribution of our galaxies. Figure 3.8 only includes the region west of the Virgo Cluster. There are only 23 galaxies in our sample east of the Virgo cluster, so the distribution in that section is not meaningful. Both figures demonstrate a high concentration of galaxies around $D = 45$ Mpc. This is apparent in both the RA and Dec projections, indicating that the concentration is probably a “wall” of galaxies. Additionally, close inspection of the spatial projections indicate that the galaxies are probably slightly more concentrated into a cluster in the region of $\alpha \approx 160^\circ$, $\delta \approx 13^\circ.5$.

The distribution of ALFALFA-only galaxies reflects the importance of the inclusion of ALFALFA data in our sample. These galaxies are only contributing to our sample beyond ~ 35 Mpc. There are two reasons why ALFALFA-only

galaxies are not contributing to our sample at closer distances. First, many of the closer detections in the ALFALFA database were eliminated from our sample because their absolute magnitude is too faint. Second, the SDSS database is, by necessity, going to be more complete at closer distances because of observational biases. Therefore, although there are real ALFALFA detections in the nearby region of space, they would also be present in Sloan or NED and not be classified as ALFALFA-only. The fact that the unique contribution from ALFALFA is occurring mostly at higher distances, where other sources of data are less complete, indicates that the inclusion of ALFALFA objects in our survey is worthwhile.

3.5 Absolute Magnitude Distribution

One major success of our sample is the distribution of absolute magnitudes that we achieve. This is best demonstrated in comparison to the well-regarded AGN survey conducted by Ho, Filippenko, & Sargent (HFS). Significantly, there are only 19 objects in our sample that were included in the HFS survey (see Table 3.1). Additionally, our sample is dominated by dwarf galaxies: it peaks at around $M_g = -15$, and falls off sharply at brighter magnitudes, while the HSF sample peaks at $M_B = -21$ (see Fig. 3.9). We have over 100 objects with $-14 < M_g < -16$ while the HFS sample has 5, none of which are in our region. This is a very promising result with regards to our ultimate goal of finding IMBHs, which we expect to dwell in dwarf galaxies.

3.6 Sample Completeness

There is currently no widely accepted luminosity function for low-luminosity galaxies, so we are not able to investigate our overall completeness at this time.

However, we are able to explore the relative completeness within our own sample as a function of distance and magnitude. Figure 3.10 explores this issue.

Our distance limit seems, in general, to be appropriate, although we begin to lose completeness for galaxies fainter than $M_g = -15.5$ for $d \lesssim 75$ Mpc. This is significant, because it indicates that our $z = 0.0177$ limit is appropriate for galaxies brighter than -15.5 . At present, we simply want to be aware of the fact that our completeness decreases at very faint magnitudes, but it should be explored in more depth for future studies. Regardless, we have achieved greater completeness of low-luminosity galaxies than other surveys have obtained, as clearly indicated in Figure 3.9.

Table 3.1: Objects from the HFS survey that are included in our sample.

Object Name (1)	Distance (Mpc) (2)	$M_{B_T}^0$ (HFS) (3)	M_g (4)	HFS Classification (5)
NGC 3338	23.12	−20.62	−19.06	H
NGC 3346	22.49	−19.51	−18.35	H
NGC 3351	8.76	−19.28	−18.31	H
NGC 3367	46.14	−21.28	−20.65	H
NGC 3368	11.79	−19.74	−19.43	L2
NGC 3377	6.94	−18.47	−16.86	E
NGC 3379	12.61	−19.36	−19.38	L2/T2
NGC 3384	11.53	−18.79	−19.04	E
NGC 3389	23.27	−19.93	−18.90	H
NGC 3412	8.75	−18.2	−18.02	E
NGC 3433	42.71	−20.82	−19.66	L2/T2
NGC 3489	6.71	−17.88	−17.32	T2/S2
NGC 3593	5.67	−17.25	−16.21	H
NGC 3596	22.66	−20.11	−19.26	H
NGC 3623	8.85	−19.67	−18.63	L2
NGC 3627	8.28	−19.97	−18.72	T2/S2
NGC 3628	8.50	−20.12	−17.21	T2
NGC 3666	15.93	−19.64	−18.25	H
NGC 3810	11.00	−20.19	−18.21	H

Col. (1): Object Name. Col. (2): Distances from our own calculations. Col. (3): $M_{B_T}^0$, from HFS. Col. (4): M_g from our own calculations. Col. (5): Classification of the nuclear spectrum as given in the HFS paper (see Sec 4.1). H = HII nucleus, E = Elliptical galaxy, S = Seyfert nucleus (type 1 or 2), L = LINER (type 1 or 2), and T = Transition object. If the classification is ambiguous, two different possible classifications are given.

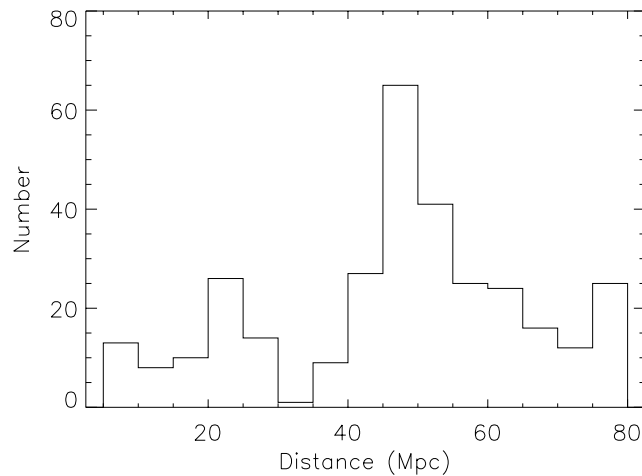


Figure 3.7: Distance distribution for the galaxies in our final sample. The width of each bin corresponds to 5 Mpc

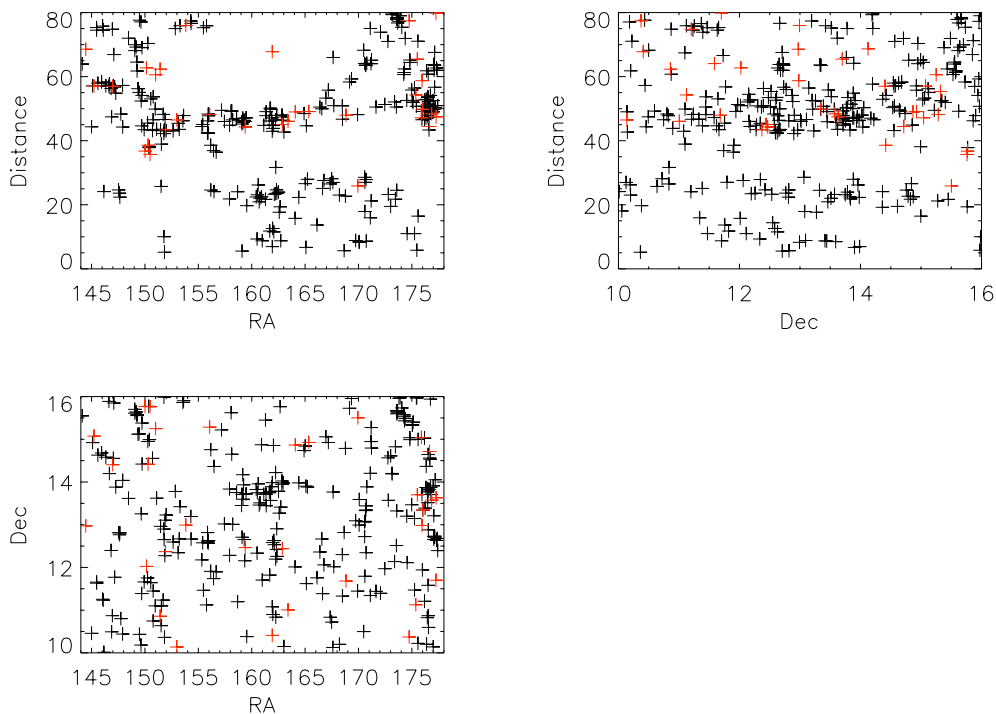


Figure 3.8: Three visualizations of the spatial distribution of our galaxies. Distances are in units of Mpc, RA and Dec are in degrees. ALFALFA-only galaxies are plotted in red.

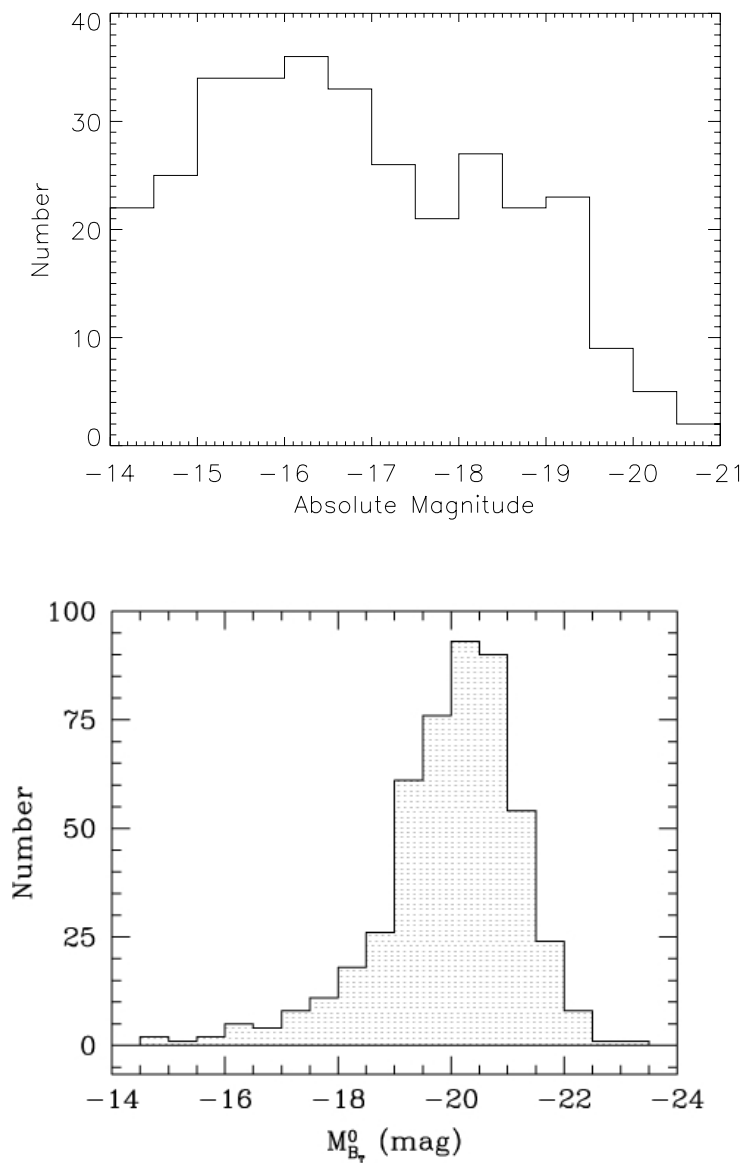


Figure 3.9: Top: absolute g -Magnitude distribution for the 319 objects in our final sample. The width of each bin corresponds to 0.5 Mag. Bottom: Absolute B -Magnitude distribution for the HFS sample (HFS 1997).

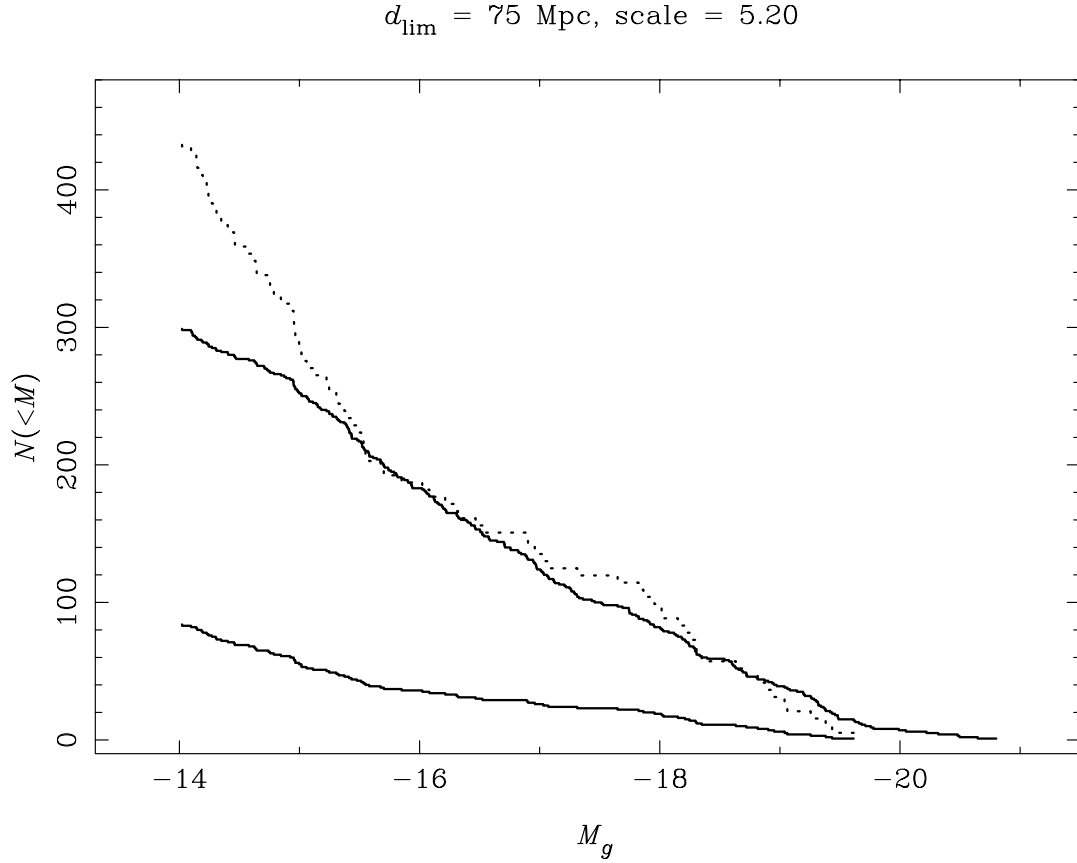


Figure 3.10: Total galaxies out to 75 Mpc (top line) as compared to galaxies at 35 Mpc or closer (bottom line). The dotted line is a scaled version of the 35 Mpc line, demonstrating the number of galaxies we would expect to find at 75 Mpc if the completeness was the same as at 35 Mpc. Lines are drawn using a cumulative counting method, such that a point at $M_g = -16$ corresponds to the total number of galaxies with magnitude of -16 or brighter. We appear to lose no completeness for galaxies brighter than $M_g \approx -15.5$ by extending our distance range from 35 Mpc to 75 Mpc.

Chapter 4

Spectroscopy

Now that the basic characteristics of our sample are established, we are ready to return to the original goal: looking for black holes. In order to determine which of our galaxies host central black holes, we need to examine their spectra. An introduction to spectral identification of AGNs and their physical properties is given in Sections 4.1 and 4.2, followed in Section 4.3 by discussion of how this was accomplished for our sample. Our results are given in Section 4.5.

4.1 Spectral Signatures of AGNs

When spectra of galaxies were first obtained, astronomers noticed that some galaxies have emission lines in their spectra, while others have only absorption features (see Appendix B for an explanation of spectral features). While the spectra of the absorption-line galaxies can easily be explained by the integrated light from many stars, the phenomena behind the emission-line spectra was initially more obscure. Some of the spectra of these “extragalactic nebulae” were similar to the emission-line spectra of planetary nebulae in our own Galaxy, while others had characteristically different patterns of emission. Carl Seyfert (1943) was one of the first people to notice that a small fraction of galaxies have nuclei whose spectra show evidence of a very high-energy source of ionization, and have broader lines than the absorption lines in other galaxies. These galaxies have spectra charac-

teristically and fundamentally different from other emission-line spectra, allowing us to classify galaxies into three categories, although we will continue to refine the significance and definitions of these categories below: (1) galaxies with no emission lines; (2) galaxies with “low energy” emission lines; (3) galaxies with high-ionization “Seyfert” emission-line spectra.

Objects in categories (1) and (2) need very little explanation. The first type of galaxies are early-type spiral or elliptical galaxies with simple stellar populations. Their spectra simply reflect the integrated light from many stars in the galaxy. The second type of galaxies have spectra that can be well modeled by photoionization of interstellar gas by young, hot O and B stars. Similar spectra are seen in the HII regions in our own Galaxy, where atoms in the interstellar medium are being photoionized by stellar activity. The galaxies in which these HII spectra are seen are primarily spiral and irregular galaxies in which there is plenty of interstellar gas and young, recently formed stars that can ionize it (Osterbrock & Ferland 2006). Although these regions of star formation and ionized gas occur in the spiral arms of all late-type galaxies, when there is a vigorous episode of star formation happening in the nucleus of the galaxy to dominate the nuclear emission with ionization from young stars, the galaxy is known as a “starburst galaxy.” For the purposes of this discussion, all galaxies in which stellar photoionization is the cause of spectral emission lines will be referred to as “HII” galaxies.

However, it is not as straightforward to explain the emission lines that are observed in the third type of galaxies. Further examination of their spectral properties will help reveal the excitation method driving the observed ionization. For now, we will refer to them as “AGN” and return to the physical causes of their spectra later. Some sample spectra can be seen in Figure 4.1.

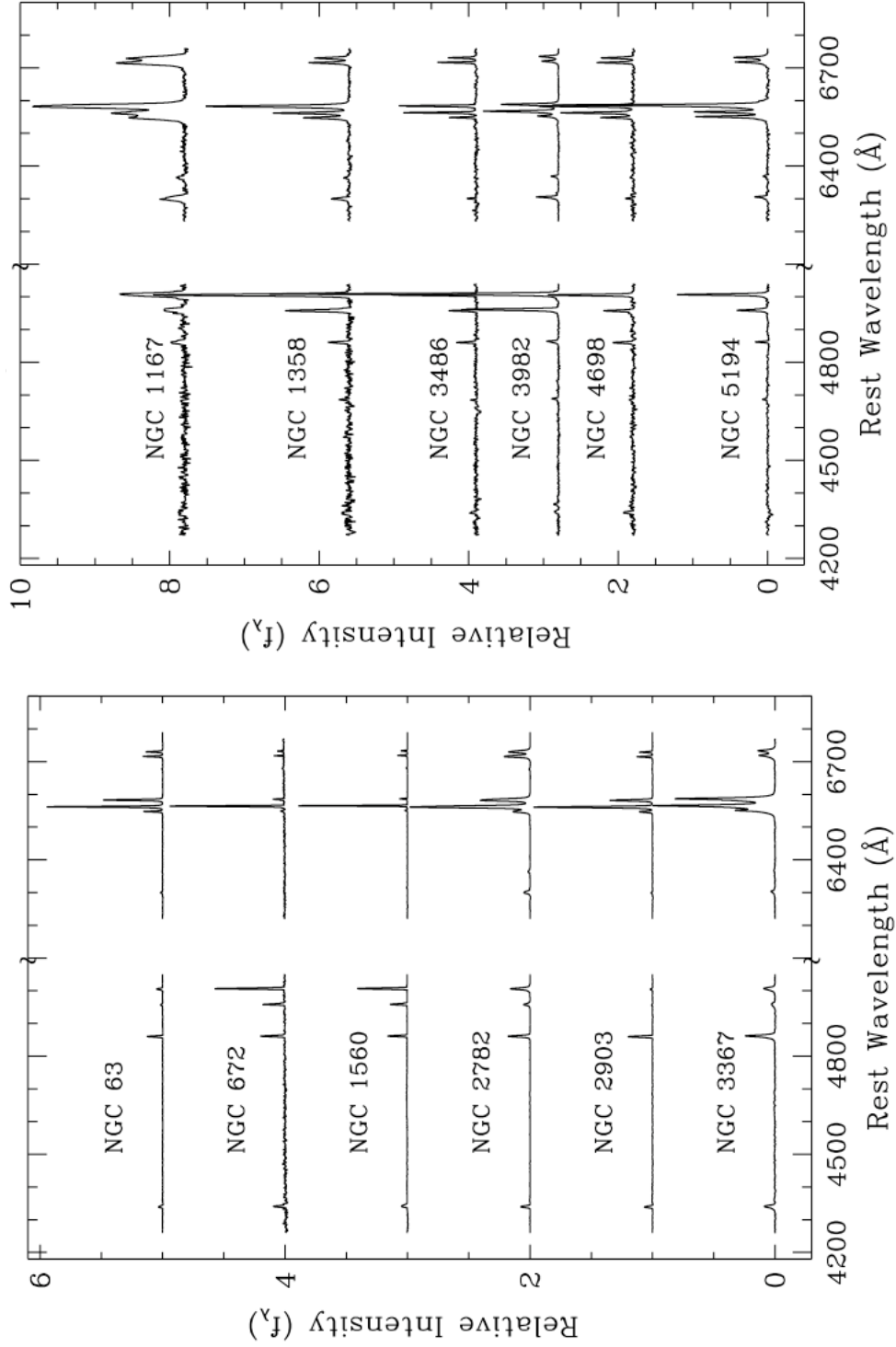


Figure 4.1: Sample spectra of HII galaxies (left) and AGN (right, spectra from HFS). From left to right, the important diagnostic lines are $H\beta$ $\lambda 4861$, $[\text{OIII}]$ $\lambda\lambda 4959, 5007$, $[\text{NII}]$ $\lambda 6548$, $H\alpha$ $\lambda 6563$, $[\text{NII}]$ $\lambda 6548$, and $[\text{SiII}]$ $\lambda\lambda 6716, 6731$.

Classification System

The first step in understanding the nature of active galaxies is to establish a firm system for distinguishing them from HII galaxies. The first such system was developed originally by Baldwin, Phillips, & Terlevich (1981, hereafter BPT), and refined by Veilleux & Osterbrock (1987). The technique relies on comparing ratios of emission lines to one another in such a way that the empirically determined differences between HII galaxies and AGN become apparent in parameter-space. The most commonly used BPT diagnostic diagrams compare the emission line ratios $[\text{OIII}]\lambda 5007/\text{H}\beta\lambda 4861$ to $[\text{NII}]\lambda 6583/\text{H}\alpha\lambda 6563$ or $[\text{SII}]\lambda\lambda 6716, 6731/\text{H}\alpha\lambda 6563$ (see Figs. 4.2, 4.3).

The choice of these line ratios is not arbitrary; the $[\text{OIII}]/\text{H}\beta$ ratio functions as an indicator of the mean level of ionization and temperature, while $[\text{NII}]/\text{H}\alpha$ and $[\text{SII}]/\text{H}\alpha$ are indicators of the relative importance of a partially ionized zone produced by very high-energy radiation (Osterbrock & Ferland 2006). In other words, galaxies with very few ionizing photons will appear towards the left side BPT diagrams, while galaxies with many of low-energy ionizing photons but few high-energy photons will appear on the upper left of the diagram. Very high-ionization galaxies lie in the upper right area of the diagram. We do not expect to find galaxies in the lower right, because such galaxies would need to have many high-energy ionizing photons, but few lower-energy ionizing photons.

It is also interesting to note that these ratios involve lines that have similar wavelengths, meaning that the ratios are mostly insensitive to the effects of interstellar reddening. Additionally, we use ratios that compare a metal line to an H I Balmer line, because Balmer lines are less sensitive to effects of elemental abundances (Veilleux & Osterbrock 1987).

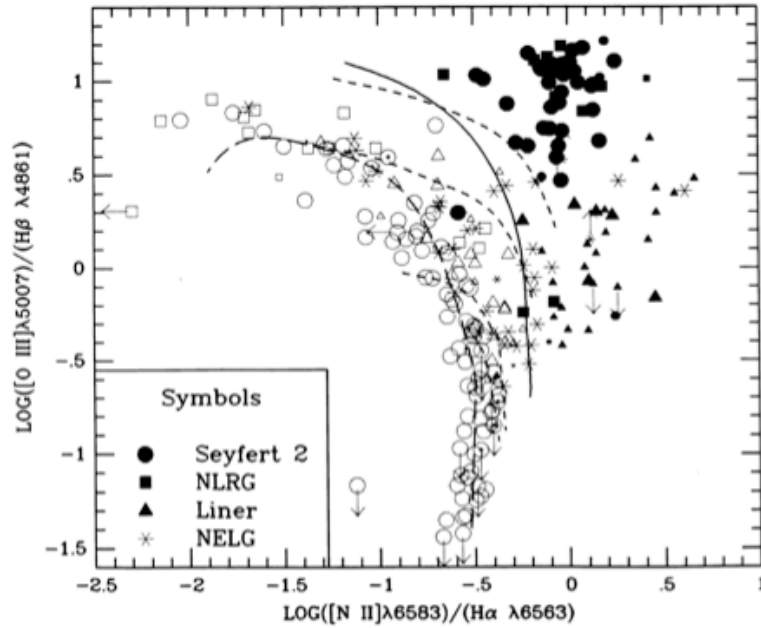


Figure 4.2: BPT diagram of $[O\text{III}]/H\beta$ versus $[N\text{II}]/H\alpha$. Open symbols are H II galaxies, solid symbols are active galaxies. The solid line is the dividing line between active galaxies and H II galaxies (from Veilleux & Osterbrock 1987).

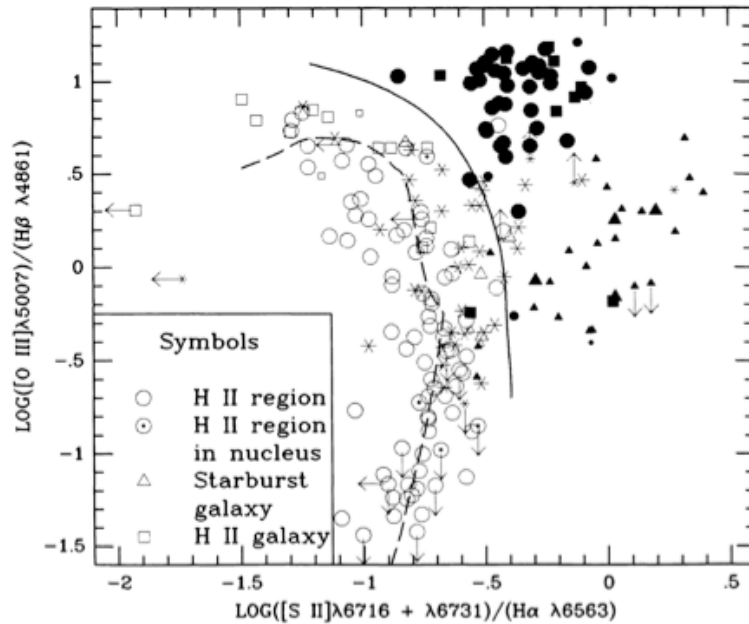


Figure 4.3: BPT diagram of $[O\text{III}]/H\beta$ versus $[S\text{II}]/H\alpha$. Symbols as in Figure 4.2 (Veilleux & Osterbrock 1987).

4.2 Physical Explanation of AGNs

These BPT diagrams definitively demonstrate that active galaxies live in an energetic regime of parameter space that is distinctly different from HII-region galaxies. The strength of their high-energy emission lines is far greater than what is found in or can be modeled by star forming regions, indicating some very high-energy source of ionizing photons. Overwhelmingly, the evidence points to accretion around a supermassive black hole as the cause of this AGN emission.

One of the key pieces of evidence for the black hole hypothesis is that variations in AGN luminosity have been observed, and such variations can occur over timescales as short as a few days. This puts a limit on the physical size of the region creating the AGN emission, because variations cannot propagate faster than the speed of light. Therefore, the high energies indicated in AGN spectra must be produced in a very concentrated region. Furthermore, the luminosity of a typical AGN ($\sim 10^{12}L_{\odot}$) is far too large for the source to be a star, whose maximum luminosities are $\sim 10^5L_{\odot}$ (Osterbrock & Ferland 2006). The physics of thermonuclear reactions puts a limit on how much energy a star can put out before it becomes too unstable to exist, so AGN luminosities cannot simply be created by “supermassive stars”. However, large energies can be produced in a small volume by gravitational release of energy, as would occur in an accretion disk around a black hole¹. Indeed, black holes are the only known phenomenon that are capable of producing the extremely concentrated (and large) amounts of energy that are observed in AGNs (Osterbrock & Ferland 2006).

¹Broad spectral lines that are observed in some (“type 1”) AGN are considered to be direct observations of this accretion disk, providing further evidence for the BH hypothesis. AGN spectra with no observed broad lines are referred to as “type 2”. It is accepted that type 2 objects do have accretion disks, but because of our line of sight, we cannot see the broad line region directly.

As a final note regarding the nature of AGNs, a distinction is usually made between galaxies exhibiting the most energetic patterns of AGN emission (the solid circles in Figs. 4.2 and 4.3), called Seyfert Galaxies, and the slightly less energetic galaxies (the solid triangles), referred to as Low-Ionization Nuclear Emission Regions² (LINERs). This distinction is made because there has been some controversy regarding the physical cause behind LINER emission (See Appendix C). While the high energy exhibited in the spectra of Seyfert galaxies leaves no doubt that only a black hole could be driving the emission, LINERs are in a slightly less energetic state, and so have the potential to be powered by something other than a black hole. However, in recent years there has been increasing evidence that black holes are the cause of LINER emission in most, if not all, LINER galaxies (e.g., Ho 2008). For the purposes of our sample, we are considering LINERs to be a type of AGN.

4.3 Obtaining the Spectra

Now that we have demonstrated the importance of spectra for classification of AGNs, we want to apply this classification system to the galaxies in our sample. We have three sources of spectra of our galaxies: SDSS, HFS, and our own observations.

Although 270 of the galaxies in our sample have SDSS spectra, only 235 of those are centered on the nucleus of the galaxy. Of 35 galaxies with no nuclear spectrum, 9 of them are HFS objects, so we can adopt the spectral classification assigned by HFS and do not need to obtain additional spectra for these objects (see Table 4.3). We use visual inspection of the raw SDSS spectra to determine

²There is a third class of galaxies, known as Transition Objects (TOs), that lie in an ambiguous area of the BPT diagram between LINERs and HII galaxies.

if the data quality is good enough to be able to determine the spectral class of the galaxy. Of the galaxies that have nuclear spectra, 35 of the SDSS spectra are contaminated by a significant to severe amount of noise that prevents us from making a spectral classification.

Therefore, from SDSS and HFS we have acceptable nuclear spectra for only 209 galaxies: 66% of our total sample. We supplement this data with our own observations in order to obtain as much spectroscopic completeness as possible.

Follow-up Spectroscopy

Our follow-up data were obtained at the Lick and MDM observatories over three observing runs in 2008 and 2009. In total, we were able to obtain spectra of 35 objects.

Lick Observatory is located on Mount Hamilton, outside of San Jose, California. Our data were obtained with the KAST spectrograph on the Shane 3-meter Telescope on March 6th – 8th 2008. We employed a 600 line mm⁻¹ diffraction grating on the red arm of the of the spectrograph, with no dichroic, providing coverage of the wavelength range 4200 – 7000 Å at 5 – 6 Å resolution (FWHM). The spectrographic slit width was 2 arcseconds.

MDM Observatory is located on the southwest ridge of Kitt Peak, outside of Tucson, Arizona. Our data were obtained with the Boller & Chivens CCD Spectrograph (CCDS) on the 2.4-meter Hiltner Telescope. Our observing runs occurred in March 3rd – 5th 2008 and February 20th – 25th 2009. We used the 150 line mm⁻¹ diffraction grating, giving us coverage of the 3700 – 7400 Å range at a resolution of 8 – 10 Å (FWHM). Second order light was suppressed with a GG350 order-blocking filter. The spectrographic slit width was 1.5 arcseconds.

At both telescopes, about a third of the observing time was lost due to cloudy conditions. Our exposure times varied depending on the brightness of the galaxies, but were generally between 600–1800s. A few very faint objects were observed for 3600s. Data were reduced and analyzed following standard procedures in IRAF.

4.4 Starlight Subtraction

The optical spectra of many emission-line galaxies are heavily contaminated, and sometimes dominated, by the stellar component of the spectra. This contamination occurs because it is impossible to completely exclude starlight from a spectral measurement, especially because the stellar density in a galaxy peaks at the nucleus. Because stellar spectra are absorption-dominated, and some of the stellar absorption features occur at the same wavelengths of the emission lines we need to measure, stellar contamination reduces the apparent strengths of some emission lines and complicates classification. Specifically, there is always some absorption of the H α Balmer lines in stellar spectra, which we use to discriminate between HII galaxies and AGNs. Therefore, we must try to remove the contamination from stars as much as possible.

Our method of starlight subtraction involves adopting a “spectral template” that represents a stellar continuum and absorption-line strength appropriate for the galaxy. Our template spectra are from SDSS, and have been confirmed to be free of emission lines. The template spectrum is first scaled to match the flux of the continuum in our emission-line spectra, then subtracted from it. The resulting spectrum should be a continuum-subtracted pure emission-line spectrum. An example of how this method works to remove the effects of stellar absorption from the H β line can be seen in Figure 4.4.

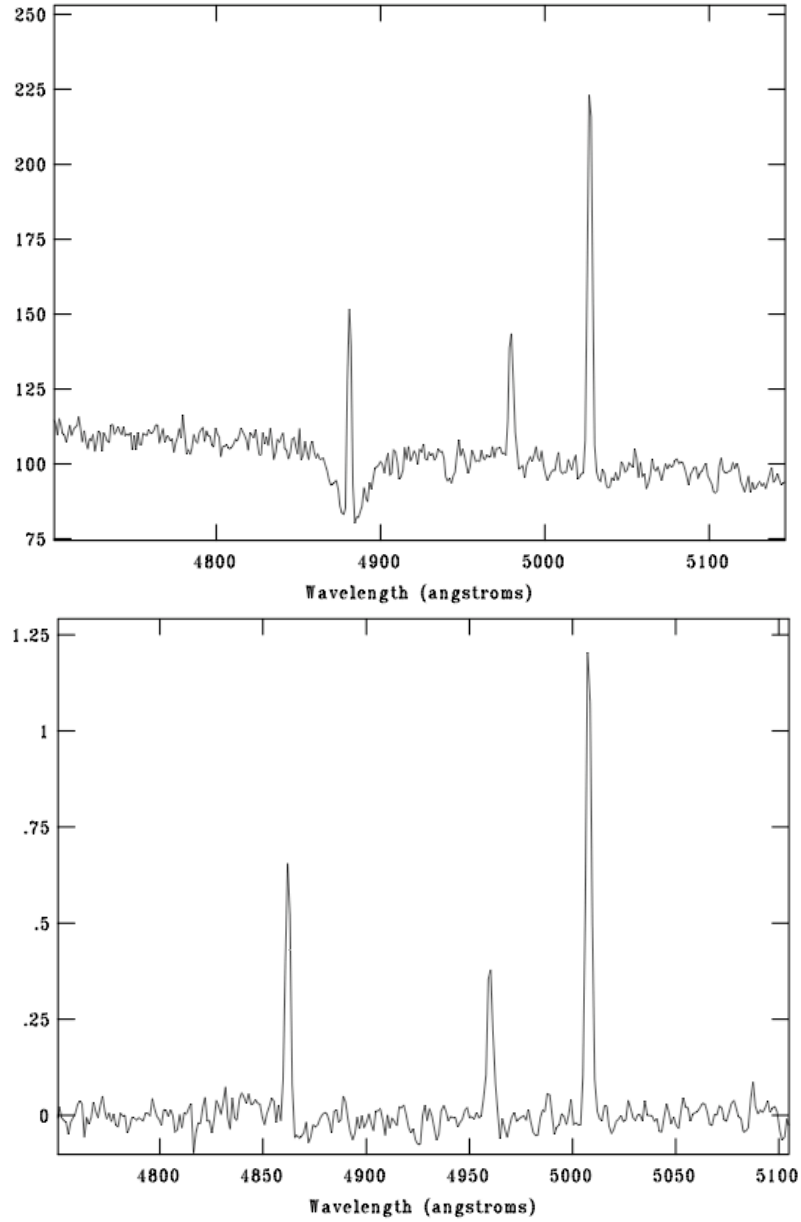


Figure 4.4: Raw spectrum (top) and starlight subtracted spectrum (bottom) for one of the objects in our sample. The continuum has been removed (although the flux calibration has changed for the starlight-subtracted spectrum), and the effects of stellar absorption have been removed. This process changes the flux of the $H\beta$ line, and therefore changes the $[OIII]/H\beta$ ratio, one of our important classification parameters. The three lines are $H\beta$ and $[OIII] \lambda\lambda 4959, 5007$.

4.5 Results from Spectroscopy

The first step in identifying the AGNs in our sample is to generate our own BPT diagrams. These are displayed in Figure 4.5. As one can see, we have 13 AGN in our sample from SDSS: 4 Seyferts and 9 LINERs. There is also one additional SDSS galaxy that is clearly an AGN, but the $[\text{OIII}]/\text{H}\beta$ ratio is too uncertain to determine whether the galaxy is a LINER or a Seyfert. We are now able to definitively classify 201 galaxies as either Seyferts, LINERs, HII galaxies, or early-type galaxies from their SDSS spectra alone. Early-type galaxies are dominated by starlight to the point where emission lines cannot be detected. However, these galaxies may have some emission that could be detected in better spectra, so they should not be completely discounted until definitive follow-up observations are made. The details for these “classifiable” SDSS galaxies are in Table 4.4. Note that Table 4.4 does not include the galaxies for which we are adopting the classification given in HFS.

There are 5 HFS objects that are classified as AGNs from the HFS sample (see Table 4.3). Additionally, from our own follow-up observations, we are able to classify 4 more galaxies as AGNs (see Table 4.2): 2 definite Seyfert galaxies, and 2 AGNs whose subtype cannot be determined with our current data (see below). In total, we have 244 galaxies whose spectra can be classified, giving us 77% total spectroscopic completeness.

There are a few cases where we cannot obtain accurate line ratios because of low signal-to-noise ratios in the original data. However, some of these galaxies are still classifiable with the information we have. For instance, object SDSSJ110426.48+114522.8 has very little N[II] emission, possibly because it was mistakenly “cleaned” from the spectrum by the SDSS pipelines. However, we can still place it on the

$[\text{OIII}]/\text{H}\beta$ vs $[\text{SII}]/\text{H}\alpha$ BPT diagram, and classify it as an HII galaxy from those ratios. Additionally, in many cases, there is very significant noise in the blue end of the spectrum, making measurements of $[\text{OIII}]$ and $\text{H}\beta$ difficult, but the $[\text{SII}]$, $[\text{NII}]$, and $\text{H}\alpha$ lines are present and measurable, with high signal-to-noise. Since $\log([\text{NII}]/\text{H}\alpha) \gtrsim -0.02$ or $\log([\text{SII}]/\text{H}\alpha) \gtrsim 0$ is a clear indication of an AGN, some galaxies can be classified as an AGN by these ratios alone, even if we cannot place them on a BPT diagram. The galaxy SDSSJ095747.77+150732.1 is one such object.

Table 4.1 provides additional information for the SDSS AGNs in our sample. Absolute magnitudes and $(g - r)$ color are given. Additionally, K -magnitudes (from the Two Micron All Sky Survey, 2MASS) are given for all but one AGN candidate, for which this information is not available. These quantities allow us to calculate the stellar mass of the AGN host galaxies based on the procedure in Bell (2003). Also given is $\text{H}\alpha$ luminosity for each SDSS AGN. $\text{H}\alpha$ luminosity gives us an approximate measure of the galaxy's nuclear luminosity, which is related to the BH mass and accretion rate. Figure 4.6 demonstrates the comparison between the luminosity properties of the AGNs in our sample and all of the AGNs found in the HFS survey. The AGNs that we have found are more concentrated towards low $\text{H}\alpha$ luminosity and absolute magnitude, in comparison to the HFS AGNs.

Significance of our Discoveries

Close inspection of Tables 4.1 and 4.2 reveals that we have successfully begun to explore the range where we expect to find IMBHs. We have a few galaxies with very low stellar masses and faint absolute magnitudes, a promising sign that the black holes responsible for the AGN emission lie in the low-mass range

for supermassive black holes. Additionally, we have identified 6 Seyfert galaxies, while the HFS sample found no Seyferts in this region of space. Future study of our newly-discovered AGNs promises to reveal fascinating information about the nature of black holes.

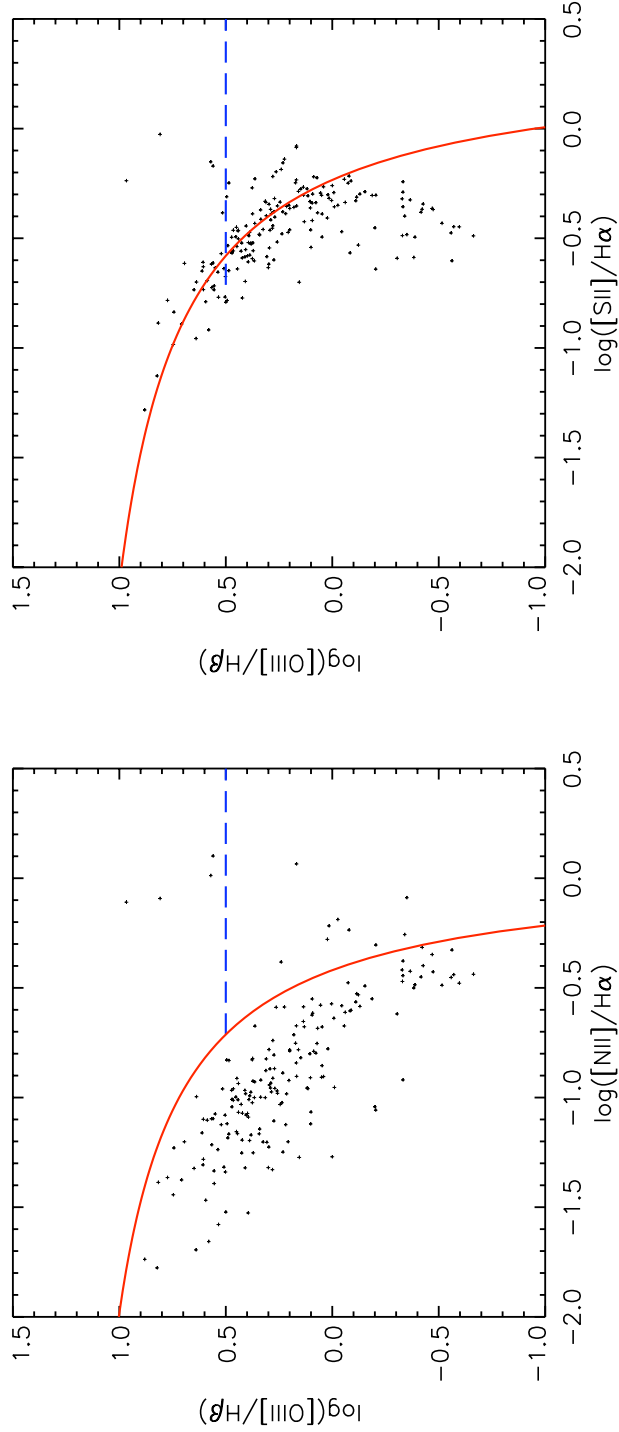


Figure 4.5: Diagnostic diagrams plotting $\log([OIII]/H\beta)$ vs. $\log([NII]/H\alpha)$ (left) and $\log([OIII]/H\beta)$ vs. $\log([SII]/H\alpha)$ (right). Blue dashed line is separation between LINERs and Seyferts, at $([OIII]/H\beta) = 3$ (from Barth et al. 2008); red line is upper limit on HII galaxies, from Kauffmann et al. (2003) on the on the $[NII]/H\alpha$ graph, and from Kewley et al. (2006) on the on the $[SII]/H\alpha$ graph. Note the Kauffmann line is a more conservative upper limit on HII galaxies than the Kewley line, which may need adjustment. For this reason, we base our classification most strongly on the $[NII]/H\alpha$ diagnostic diagram, although the $[SII]/H\alpha$ diagram confirms our classifications.

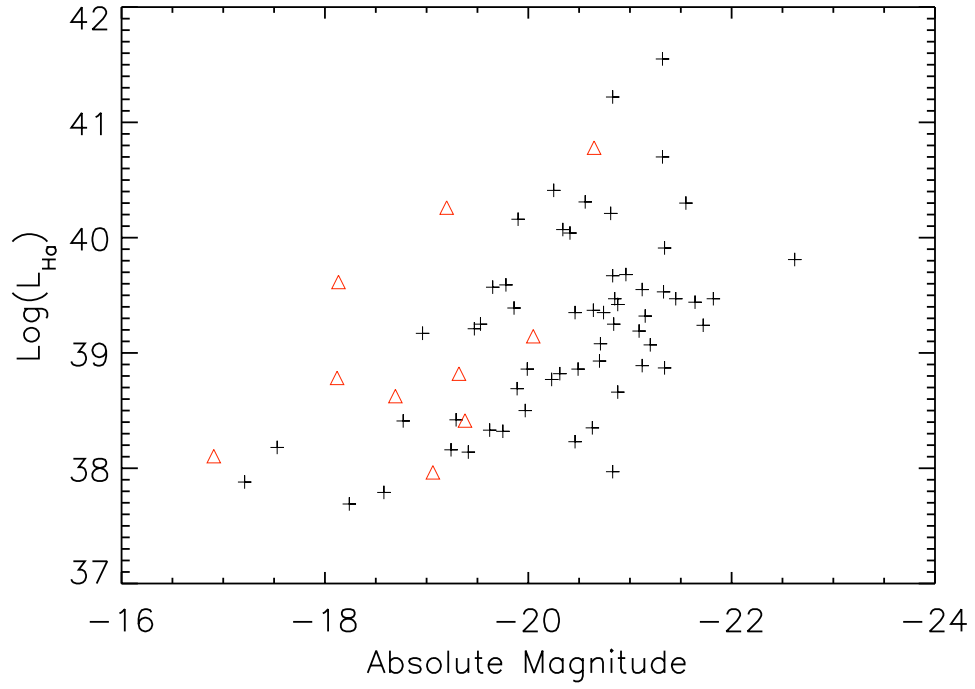


Figure 4.6: Total galaxy magnitude vs. nuclear H α luminosity for all of the HFS AGNs (black crosses) and our AGNs (red triangles). Absolute Magnitude for the HFS objects are derived using original B -band magnitudes.

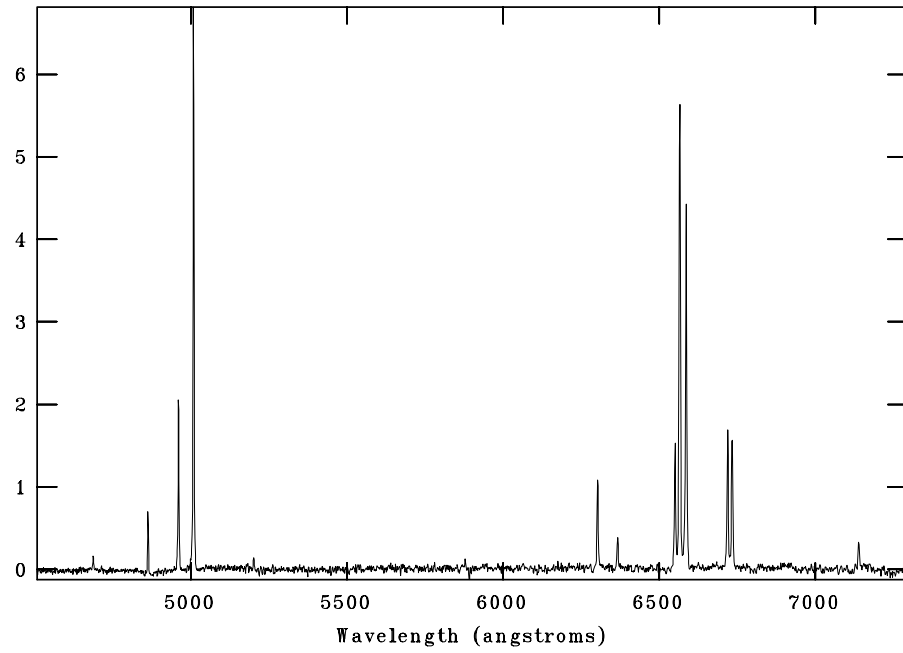


Figure 4.7: The spectrum of SDSSJ100551.19+125740.6, one of the new Seyferts in our sample. The image of the galaxy can be seen in Fig. 4.8.

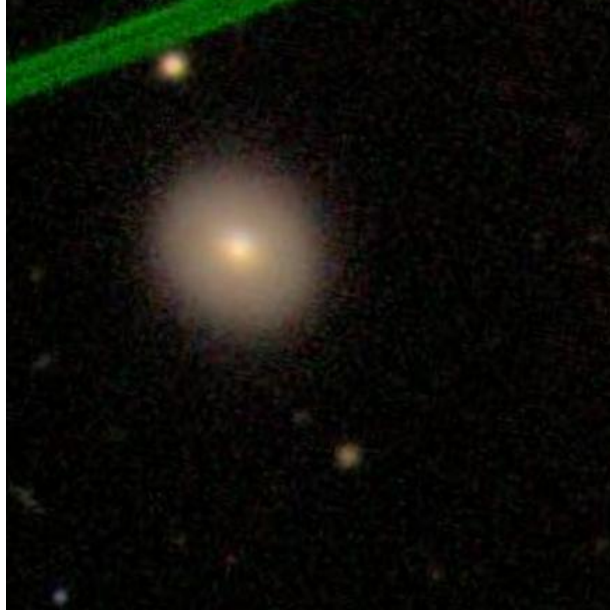


Figure 4.8: SDSS image of SDSSJ100551.19+125740.6, one of the new Seyferts in our sample. The spectrum of the galaxy can be seen in Fig. 4.7. The green line is a flaw in the image.

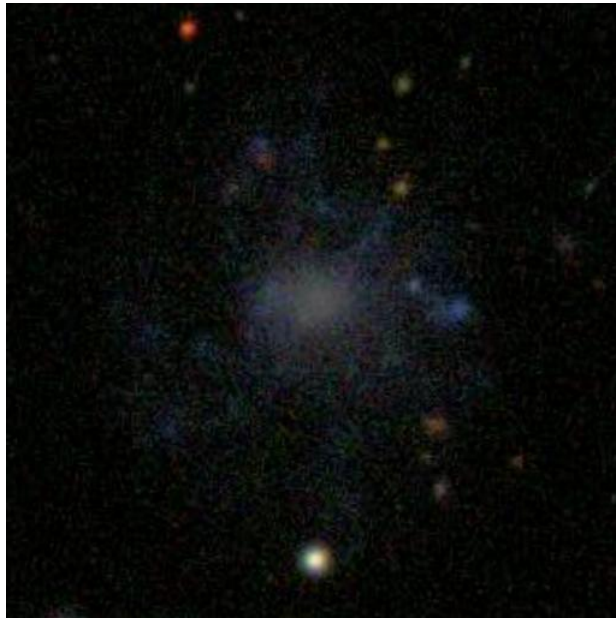


Figure 4.9: SDSS image of SDSSJ112912.36+115153.1, one of the new Seyferts in our sample. It is interesting to note this galaxy's morphological resemblance to NGC 4395, the prototypical dwarf AGN.

Table 4.1: Properties of the SDSS AGNs in our sample.

Object Name (1)	M_g (2)	$(g-r)$ (3)	m_K (4)	Classification (5)	$\log M_\star$ (6)	$\log L_{H\alpha}$ (7)
SDSSJ094408.53+111514.8	-18.12	0.802	12.42	S	10.640	38.784
SDSSJ095703.24+153441.7	-18.69	0.442	...	L	...	38.625
SDSSJ095747.77+150732.1	-19.38	0.805	10.73	AGN	11.038	38.414
SDSSJ100551.19+125740.6	-18.13	0.714	11.41	S	10.540	39.615
SDSSJ104207.53+134449.1	-19.06	0.731	8.13	S	11.310	37.964
SDSSJ104634.95+134503.0	-20.65	0.725	8.76	L	11.660	40.780
SDSSJ111436.99+124903.6	-16.91	1.033	7.42	L	10.434	38.105
SDSSJ114009.38+151938.2	-19.32	0.455	11.10	S	10.779	38.820
SDSSJ114139.73+155756.5	-19.20	0.767	10.39	L	11.098	40.261
SDSSJ114545.56+104928.4	-20.05	0.885	9.21	L	11.541	39.145
SDSSJ114058.75+112816.1	-18.21	0.687	7.95	L	10.728	36.713
SDSSJ104741.47+110437.4	-19.34	0.541	10.26	L	10.958	36.015
SDSSJ112426.06+112031.9	-18.25	0.622	9.23	L	10.527	34.827

Col. (1): Galaxy name. Col. (2): Apparent g -magnitude. Col. (3): $(g-r)$ color. Col. (4): K-Magnitude, from the 2MASS Survey. Col. (5): Galaxy classification, S=Seyfert, L=LINER, AGN=active galaxy of indeterminate type. Col. (6): log of the stellar mass in units of solar masses. Col. (7): log of the $H\alpha$ luminosity, in ergs s^{-1} .

Table 4.2: Properties of the AGNs found by follow-up observations.

Object Name (1)	M_g (2)	$(g-r)$ (3)	m_K (4)	Classification (5)	$\log M_\star$ (6)
SDSS J100422.48+133716.9	-19.26	-2.88	10.34	AGN	10.27
SDSSJ105117.69+135645.9	-19.78	0.59	10.28	AGN	11.05
SDSSJ112912.36+115153.1	-17.03	0.16	...	S	...
SDSSJ114827.49+124337.9	-19.48	0.67	11.18	S	10.95

Col. (1): Galaxy name. Col. (2): Apparent g -magnitude. Col. (3): $(g-r)$ color. Col. (4): K-Magnitude, from the 2MASS Survey. Col. (5): Galaxy classification, S=Seyfert, AGN=active galaxy of indeterminate type. Col. (6): \log of the stellar mass in units of solar masses.

Table 4.3: AGNs in our region from the HFS sample.

Name (1)	Distance (Mpc) (2)	m_g (3)	M_g (4)	$(g - r)$ (5)	m_K (6)	$\log M_\star$ (7)	Classification (8)
NGC 3489	6.71	11.82	-17.32	1.160	7.37	10.62	T2/S2
NGC 3627	8.28	10.87	-18.72	0.852	5.881	11.34	T2/S2
NGC 3379	12.61	11.12	-19.38	0.816	6.27	11.55	L2/T2
NGC 3368	11.79	10.92	-19.43	0.838	6.32	11.47	L2
NGC 3623	8.85	11.10	-18.63	0.930	6.066	11.34	L2

Col. (1): Galaxy name. Col. (2): Distance, as calculated in Section 3.1. Col. (3): Apparent g -magnitude, from SDSS. Col. (4): Absolute g -mag. Col. (5): $(g - r)$ color. Col. (6): K -Magnitude, from the 2MASS Survey. Col. (7): \log of the stellar mass in units of solar masses. Col. (8): Galaxy classification, as given in HFS.

TABLE 4.4
Distances, Magnitudes, and Spectral Classification of SDSS Galaxies

Galaxy Name (1)	D (Mpc) (2)	m_g (3)	M_g (4)	$\log[\text{OIII}]/\text{H}\beta$ (5)	$\log[\text{NII}]/\text{H}\alpha$ (6)	$\log[\text{SII}]/\text{H}\alpha$ (7)	Classification (8)
SDSSJ093630.58+153255.5	63.93	16.82	-17.21	0.289	-0.957	-0.368	H
SDSSJ094024.09+145521.4	57.13	13.29	-20.49	...	0.741	0.517	H
SDSSJ094153.90+113916.2	74.51	18.42	-15.94	0.566	-1.216	-0.725	H
SDSSJ094153.93+113757.0	75.31	17.12	-17.26	0.069	-0.685	-0.384	H
SDSSJ094223.36+143748.2	57.94	15.87	-17.95	0.442	-1.011	-0.467	H
SDSSJ094345.73+144047.9	58.29	17.25	-16.57	0.077	-0.798	-0.338	H
SDSSJ094408.53+111514.8	75.78	16.28	-18.12	0.808	-0.093	-0.027	S
SDSSJ094423.49+111352.6	74.52	15.04	-19.32	-0.427	-0.399	-0.344	H
SDSSJ094521.39+143447.7	57.16	17.67	-16.12	0.398	-1.073	-0.580	H
SDSSJ094631.02+155310.7	56.95	15.47	-18.31	-0.332	-0.444	-0.290	H
SDSSJ094640.92+141151.9	57.66	16.86	-16.94	0.232	-0.888	-0.380	H
SDSSJ094719.94+122347.3	56.31	17.35	-16.40	0.172	-0.753	-0.247	H
SDSSJ094731.39+102931.5	47.46	17.95	-15.43	0.258	-0.970	-0.517	H
SDSSJ094748.15+105212.1	74.81	17.21	-17.16	0.521	-1.124	-0.570	H
SDSSJ094810.89+143313.2	57.04	18.37	-15.41	0.041	-0.905	-0.265	H
SDSSJ094820.28+155054.8	66.89	18.23	-15.90	0.314	-1.000	-0.331	H
SDSSJ094839.30+114610.0	56.80	17.01	-16.76	0.472	-0.967	-0.496	H
SDSSJ094904.73+135250.1	54.84	16.01	-17.69	0.382	-0.976	-0.522	H
SDSSJ095006.64+124848.9	24.63	14.00	-17.95	0.092	-0.616	-0.299	H
SDSSJ095027.39+124555.7	23.64	13.84	-18.03	0.200	-0.783	-0.462	H
SDSSJ095036.25+124832.6	22.39	16.73	-15.02	0.158	-0.782	-0.286	H
SDSSJ095058.82+104805.7	48.33	15.68	-17.74	-0.154	-0.492	-0.288	H
SDSSJ095138.19+102622.9	57.24	18.21	-15.58	0.500	-1.522	-0.792	H
SDSSJ095140.51+140217.3	44.26	15.90	-17.33	0.387	-0.992	-0.577	H
SDSSJ095351.48+133654.3	71.99	15.14	-19.14	-0.383	-0.501	-0.588	H
SDSSJ095611.97+154203.1	69.96	16.46	-17.77	0.587	-1.104	-0.693	H

TABLE 4.4 – *Continued*

Galaxy Name (1)	D (Mpc) (2)	m_g (3)	M_g (4)	$\log[\text{OIII}]/\text{H}\beta$ (5)	$\log[\text{NII}]/\text{H}\alpha$ (6)	$\log[\text{SII}]/\text{H}\alpha$ (7)	Classification (8)
SDSSJ095612.70+153637.0	68.13	18.52	-15.64	0.274	-1.107	-0.599	H
SDSSJ095700.36+153320.3	64.54	16.30	-17.75	-0.330	-0.471	-0.488	H
SDSSJ095703.24+153441.7	61.76	15.26	-18.69	0.239	-0.382	-0.186	L
SDSSJ095724.42+150701.5	56.22	17.71	-16.04	-0.057	-0.673	-0.231	H
SDSSJ095747.77+150732.1	55.08	14.33	-19.38	...	0.405	0.457	H
SDSSJ095756.69+102556.8	77.62	14.89	-19.56	-1.385	H
SDSSJ095836.23+131518.9	52.41	14.73	-18.87	0.279	-0.740	-0.443	H
SDSSJ095847.13+112319.3	44.64	15.33	-17.91	0.047	-0.678	-0.389	H
SDSSJ095853.33+152247.8	69.04	15.11	-19.08	-0.516	-0.489	-0.432	H
SDSSJ095943.49+113938.6	43.45	14.51	-18.68	0.730	-0.276	-0.937	H
SDSSJ100058.57+114514.5	45.49	17.89	-15.40	0.257	-0.981	-0.352	H
SDSSJ100105.15+145651.4	70.36	16.80	-17.43	0.309	-0.824	-0.397	H
SDSSJ100139.70+145931.4	38.13	17.94	-14.97	0.408	-1.321	-0.697	H
SDSSJ100210.38+113836.4	53.06	17.44	-16.18	0.440	-1.068	-0.503	H
SDSSJ100251.01+143311.6	43.17	17.27	-15.90	0.508	-1.318	-0.638	H
SDSSJ100303.46+104445.4	46.55	15.15	-18.19	-0.130	-0.585	-0.299	H
SDSSJ100305.55+112646.9	53.70	16.61	-17.03	0.270	-0.959	-0.404	H
SDSSJ100351.86+110600.2	49.88	17.55	-15.94	0.325	-1.203	-0.460	H
SDSSJ100551.19+125740.6	43.29	15.05	-18.13	0.966	-0.109	-0.237	S
SDSSJ100603.82+103815.4	25.72	16.74	-15.31	0.605	-1.099	-0.630	H
SDSSJ100610.83+110601.6	38.94	16.06	-16.89	0.743	-1.230	-0.837	H
SDSSJ100649.54+111408.9	48.21	17.90	-15.52	0.637	-0.996	-0.700	H
SDSSJ100706.51+125351.3	42.24	17.74	-15.39	0.649	-1.323	-0.735	H
SDSSJ100707.17+155902.6	10.05	15.37	-14.64	0.168	-0.842	-0.086	H
SDSSJ100710.98+123904.8	43.15	15.91	-17.26	0.485	-1.167	-0.648	H
SDSSJ100727.69+121628.2	43.48	14.22	-18.97	-0.045	-0.581	-0.470	H
SDSSJ100757.12+131338.6	43.07	16.16	-17.01	0.341	-1.144	-0.485	H

TABLE 4.4 – *Continued*

Galaxy Name (1)	D (Mpc) (2)	m_g (3)	M_g (4)	$\log[\text{OIII}]/\text{H}\beta$ (5)	$\log[\text{NII}]/\text{H}\alpha$ (6)	$\log[\text{SII}]/\text{H}\alpha$ (7)	Classification (8)
SDSSJ101033.92+123539.7	43.10	17.77	-15.41	0.101	-1.120	-0.462	H
SDSSJ101123.43+134641.7	75.02	16.90	-17.48	0.375	-0.828	-0.270	H
SDSSJ101227.02+122037.4	45.43	16.83	-16.46	0.881	-1.738	-1.283	H
SDSSJ101308.96+132519.4	75.90	17.91	-16.49	0.114	-0.960	-0.307	H
SDSSJ101413.06+155142.2	46.23	16.80	-16.52	0.364	-0.929	-0.433	H
SDSSJ101428.57+155410.5	47.84	15.18	-18.22	0.135	-0.653	-0.267	H
SDSSJ101712.71+131131.3	77.37	15.49	-18.95	-0.417	-0.450	-0.381	H
SDSSJ101717.57+123951.0	76.64	18.16	-16.26	0.102	-0.910	-0.362	H
SDSSJ102138.24+123434.0	45.08	15.20	-18.07	...	0.224	0.447	H
SDSSJ102154.57+112755.8	75.28	16.80	-17.58	0.448	-0.913	-0.538	H
SDSSJ102304.63+110719.2	75.89	18.09	-16.31	0.000	-1.270	-0.260	H
SDSSJ102339.36+123725.5	42.38	17.52	-15.61	0.180	-0.714	-0.359	H
SDSSJ102437.27+115429.0	38.58	16.91	-16.02	0.218	-1.124	-0.388	H
SDSSJ102440.11+144524.3	24.59	15.05	-16.90	-0.088	-0.602	-0.239	H
SDSSJ102553.08+142147.3	24.10	14.05	-17.86	-0.075	-0.477	-0.249	H
SDSSJ102641.98+115350.0	36.43	17.37	-15.43	0.307	-1.204	-0.584	H
SDSSJ102840.48+151313.7	49.47	18.22	-15.25	0.371	-1.252	-0.557	H
SDSSJ102946.78+130105.4	46.00	14.66	-18.66	-0.367	-0.425	-0.325	H
SDSSJ103140.82+135005.7	21.82	16.32	-15.37	0.342	-1.166	-0.482	H
SDSSJ103142.10+121656.6	44.84	17.74	-15.52	0.464	-0.960	-0.464	H
SDSSJ103216.86+153718.2	49.20	17.53	-15.93	0.817	-1.387	-0.887	H
SDSSJ103230.97+143902.0	49.26	17.97	-15.49	0.047	-0.855	-0.495	H
SDSSJ103253.18+130031.7	46.50	18.26	-15.08	0.281	-1.329	-0.454	H
SDSSJ103442.80+111150.4	24.07	13.61	-18.30	-0.423	-0.316	-0.368	H
SDSSJ103612.79+132658.3	45.93	16.89	-16.42	0.375	-1.024	-0.593	H
SDSSJ103645.63+133545.2	45.67	17.91	-15.39	0.207	-1.202	-0.473	H
SDSSJ103656.76+135603.1	46.30	17.20	-16.13	0.167	-0.904	-0.353	H

TABLE 4.4 – *Continued*

Galaxy Name (1)	D (Mpc) (2)	m_g (3)	M_g (4)	$\log[\text{OIII}]/\text{H}\beta$ (5)	$\log[\text{NII}]/\text{H}\alpha$ (6)	$\log[\text{SII}]/\text{H}\alpha$ (7)	Classification (8)
SDSSJ103723.35+120923.6	46.01	15.39	-17.92	0.168	-0.673	-0.234	H
SDSSJ103807.99+102251.0	19.72	14.40	-17.07	0.273	-0.806	-0.379	H
SDSSJ104200.36+122005.7	9.32	15.75	-14.10	0.493	-1.119	-0.784	H
SDSSJ104207.53+134449.1	23.12	12.76	-19.06	0.559	0.101	-0.171	S
SDSSJ104248.44+132735.4	20.93	13.95	-17.65	0.135	-0.586	-0.304	H
SDSSJ104338.90+145218.6	22.49	13.41	-18.35	-0.571	-0.440	-0.447	H
SDSSJ104357.69+114213.6	8.76	11.41	-18.31	-0.563	-0.328	-0.603	H
SDSSJ104431.01+134240.3	44.80	17.72	-15.54	0.639	-1.695	-0.957	H
SDSSJ104509.83+152659.4	21.69	16.57	-15.11	0.773	-1.365	-0.783	H
SDSSJ104521.45+134251.1	47.81	16.34	-17.06	0.567	-1.097	-0.618	H
SDSSJ104634.95+134503.0	46.14	12.67	-20.65	-0.351	-0.089	-0.484	L
SDSSJ104653.98+134645.7	50.18	17.71	-15.79	0.822	-1.777	-1.128	H
SDSSJ104702.76+133401.5	49.81	17.16	-16.33	0.485	-0.831	-0.248	H
SDSSJ104727.43+135323.1	47.09	16.86	-16.51	0.203	-0.923	-0.350	H
SDSSJ104741.47+110437.4	42.95	13.82	-19.34	-0.079	-0.236	-0.217	L
SDSSJ104753.93+105352.1	43.85	15.75	-17.46	0.366	-1.000	-0.603	H
SDSSJ104808.53+145116.4	44.89	17.20	-16.06	0.335	-0.921	-0.414	H
SDSSJ104827.90+123159.4	23.27	12.93	-18.90	-0.559	-0.453	-0.476	H
SDSSJ104921.71+125420.1	47.92	17.59	-15.82	0.425	-1.253	-0.522	H
SDSSJ104926.70+121528.0	23.60	17.29	-14.58	0.555	-1.335	-0.735	H
SDSSJ105001.79+134705.1	23.95	16.90	-15.00	0.501	-1.339	-0.674	H
SDSSJ105119.93+140124.3	48.00	14.68	-18.72	0.094	-0.551	-0.419	H
SDSSJ105738.14+135844.5	22.28	17.50	-14.24	0.143	-1.499	-1.004	H
SDSSJ105935.63+144407.7	48.48	17.35	-16.07	0.694	-1.202	-0.615	H
SDSSJ110027.84+113715.1	44.66	17.32	-15.93	0.496	-0.829	-0.311	H
SDSSJ110426.48+114522.8	13.68	16.22	-14.46	0.556	-1.681	-0.678	H
SDSSJ110532.03+122143.2	50.50	17.47	-16.05	-0.201	-1.042	-0.453	H

TABLE 4.4 – *Continued*

Galaxy Name (1)	D (Mpc) (2)	m_g (3)	M_g (4)	$\log[\text{OIII}]/\text{H}\beta$ (5)	$\log[\text{NII}]/\text{H}\alpha$ (6)	$\log[\text{SII}]/\text{H}\alpha$ (7)	Classification (8)
SDSSJ110615.73+123956.8	49.96	18.22	-15.27	0.298	-1.226	-0.618	H
SDSSJ110632.10+112307.5	25.11	13.10	-18.90	-0.140	H
SDSSJ110703.35+120336.1	27.58	14.38	-17.82	-0.333	-0.378	-0.242	H
SDSSJ110747.04+150331.4	53.28	17.82	-15.81	0.292	-0.870	-0.464	H
SDSSJ110842.44+145530.4	55.79	17.51	-16.22	0.312	-0.877	-0.337	H
SDSSJ110955.93+104314.9	28.15	13.30	-18.95	-0.084	-0.605	-0.567	H
SDSSJ111025.21+100731.2	26.98	16.07	-16.08	0.300	-1.320	-0.634	H
SDSSJ111045.21+120058.1	50.95	13.86	-19.68	-0.597	-0.479	-0.448	H
SDSSJ111356.50+121803.8	50.89	13.78	-19.76	-0.664	-0.438	-0.489	H
SDSSJ111436.99+124903.6	5.67	12.55	-16.21	0.023	-0.279	-0.408	L
SDSSJ111638.77+154338.3	58.33	15.29	-18.54	0.094	-0.624	-0.340	H
SDSSJ111721.16+155714.6	59.29	17.52	-16.34	0.605	-1.282	-0.734	H
SDSSJ111938.66+112643.3	48.15	18.00	-15.42	0.388	-1.196	-0.473	H
SDSSJ112017.01+133522.8	8.50	12.44	-17.21	0.015	-0.217	-0.318	L
SDSSJ112156.76+102955.3	68.24	16.92	-17.25	0.394	-1.526	-0.608	H
SDSSJ112217.91+124321.1	64.11	16.03	-18.00	0.263	-0.589	-0.197	H
SDSSJ112218.55+130354.1	28.57	14.97	-17.31	0.407	-0.983	-0.552	H
SDSSJ112223.18+130440.1	27.00	17.42	-14.74	0.100	-1.066	-0.542	H
SDSSJ112223.40+114738.1	17.89	16.96	-14.30	0.537	-1.238	-0.655	H
SDSSJ112239.99+131949.9	63.67	15.44	-18.58	0.441	-0.936	-0.464	H
SDSSJ112244.49+132043.3	63.49	16.90	-17.11	0.594	-1.469	-0.789	H
SDSSJ112250.67+122041.5	27.88	16.65	-15.58	0.554	-1.392	-0.717	H
SDSSJ112306.80+135312.5	64.16	17.45	-16.59	0.148	-0.819	-0.275	H
SDSSJ112424.77+141211.1	75.03	17.85	-16.52	0.288	-0.934	-0.417	H
SDSSJ112426.06+112031.9	15.93	12.76	-18.25	-0.205	-0.305	-0.304	L
SDSSJ112440.32+145647.4	64.05	15.23	-18.81	-0.329	-0.418	-0.320	H
SDSSJ112444.50+151631.4	21.20	16.67	-14.96	0.381	-1.171	-0.527	H

TABLE 4.4 – *Continued*

Galaxy Name (1)	D (Mpc) (2)	m_g (3)	M_g (4)	$\log[\text{OIII}]/\text{H}\beta$ (5)	$\log[\text{NII}]/\text{H}\alpha$ (6)	$\log[\text{SII}]/\text{H}\alpha$ (7)	Classification (8)
SDSSJ112451.16+144744.8	65.12	17.09	-16.98	0.285	-0.974	-0.387	H
SDSSJ112634.04+112624.2	50.50	14.89	-18.62	-0.115	-0.527	-0.313	H
SDSSJ112814.61+112339.7	73.86	17.05	-17.29	0.200	-0.788	-0.364	H
SDSSJ113108.88+133413.4	23.22	17.69	-14.14	-0.204	-1.058	-0.641	H
SDSSJ113201.92+143638.8	19.50	16.22	-15.23	-0.010	-0.954	-0.356	H
SDSSJ113331.46+120814.3	52.10	16.30	-17.29	0.055	-0.579	-0.294	H
SDSSJ113350.06+144928.2	21.74	16.93	-14.76	0.422	-1.194	-0.590	H
SDSSJ113418.16+153545.4	77.86	16.08	-18.38	0.611	-1.161	-0.650	H
SDSSJ113419.55+131919.1	24.51	15.42	-16.52	0.336	-0.999	-0.371	H
SDSSJ113421.24+153937.4	78.48	14.68	-19.80	0.003	-0.573	-0.328	H
SDSSJ113438.61+153717.9	76.76	17.54	-16.88	0.452	-0.998	-0.493	H
SDSSJ113508.28+155731.0	77.26	16.06	-18.38	-0.061	-0.612	-0.337	H
SDSSJ113536.39+155830.1	79.01	16.25	-18.24	0.410	-0.968	-0.586	H
SDSSJ113612.91+154359.3	75.41	17.86	-16.53	0.445	-1.165	-0.640	H
SDSSJ113656.86+153144.2	60.65	16.39	-17.53	0.549	-1.075	-0.635	H
SDSSJ113701.89+153414.1	61.30	14.57	-19.36	-0.474	-0.427	-0.369	H
SDSSJ113730.73+152910.8	71.92	15.69	-18.60	0.131	-0.677	-0.424	H
SDSSJ113804.18+131159.9	52.57	17.17	-16.43	0.087	-0.790	-0.220	H
SDSSJ113913.53+150215.7	64.44	17.20	-16.84	0.450	-1.156	-0.450	H
SDSSJ113914.72+145932.7	65.20	15.79	-18.28	-0.389	-0.486	-0.495	H
SDSSJ114009.38+151938.2	52.45	14.28	-19.32	0.570	0.012	-0.152	S
SDSSJ114027.35+152404.4	51.93	16.60	-16.97	0.050	-0.908	-0.304	H
SDSSJ114057.48+130842.2	56.44	17.37	-16.39	0.404	-1.080	-0.444	H
SDSSJ114058.75+112816.1	11.00	12.00	-18.21	-0.026	-0.189	-0.350	L
SDSSJ114139.73+155756.5	50.74	14.33	-19.20	-0.340	-0.257	-0.399	L
SDSSJ114150.64+155825.4	5.82	14.60	-14.23	0.422	-1.072	-0.772	H
SDSSJ114215.61+101322.3	71.06	17.95	-16.31	0.428	-1.032	-0.559	H

TABLE 4.4 – *Continued*

Galaxy Name (1)	D (Mpc) (2)	m_g (3)	M_g (4)	$\log[\text{OIII}]/\text{H}\beta$ (5)	$\log[\text{NII}]/\text{H}\alpha$ (6)	$\log[\text{SII}]/\text{H}\alpha$ (7)	Classification (8)
SDSSJ114219.02+145946.3	16.47	16.73	-14.35	0.155	-1.273	-0.701	H
SDSSJ114346.11+134227.2	46.53	16.45	-16.89	-0.123	-0.532	-0.531	H
SDSSJ114356.53+115626.1	49.15	16.76	-16.70	0.393	-1.089	-0.520	H
SDSSJ114406.98+132027.1	49.81	18.15	-15.34	0.236	-1.024	-0.480	H
SDSSJ114443.48+111226.3	46.70	17.23	-16.12	0.606	-1.307	-0.610	H
SDSSJ114444.05+150140.0	52.75	18.09	-15.52	0.515	-0.961	-0.384	H
SDSSJ114529.60+101205.8	61.81	17.14	-16.82	0.471	-1.043	-0.568	H
SDSSJ114545.56+104928.4	47.81	13.35	-20.05	0.168	0.065	-0.080	L
SDSSJ114555.09+133058.5	53.76	16.29	-17.36	-0.111	-0.565	-0.329	H
SDSSJ114556.12+135021.0	51.40	16.48	-17.08	0.020	-0.778	-0.302	H
SDSSJ114603.18+143837.6	49.56	17.80	-15.68	0.224	-0.587	-0.139	H
SDSSJ114604.05+113452.7	47.22	15.47	-17.90	0.470	-1.009	-0.563	H
SDSSJ114606.18+105216.2	60.77	17.27	-16.64	0.465	-1.013	-0.557	H
SDSSJ114612.35+103543.9	49.25	14.85	-18.61	0.297	-0.781	-0.345	H
SDSSJ114639.39+143337.4	50.73	17.79	-15.74	0.271	-0.868	-0.319	H
SDSSJ114646.27+143158.9	50.32	14.91	-18.60	-0.008	-0.639	-0.292	H
SDSSJ114706.35+134224.5	49.30	13.98	-19.48	-0.470	-0.348	-0.364	H
SDSSJ114758.64+135438.4	49.03	16.74	-16.71	0.105	-0.801	-0.333	H
SDSSJ114759.03+100825.8	52.54	18.17	-15.44	0.363	-0.675	-0.229	H
SDSSJ114812.79+131233.7	49.83	15.09	-18.39	-0.305	-0.619	-0.592	H
SDSSJ114817.89+124333.1	63.73	17.89	-16.13	-0.333	-0.920	-0.357	H
SDSSJ114830.66+124347.2	56.69	16.02	-17.74	0.071	-0.754	-0.224	H
SDSSJ114832.44+124219.0	67.55	15.91	-18.24	-0.188	-0.550	-0.305	H
SDSSJ114912.23+123753.7	62.70	17.79	-16.20	0.118	-0.957	-0.274	H
SDSSJ114930.72+124037.5	61.97	16.16	-17.80	0.374	-0.822	-0.389	H
SDSSJ114940.09+122338.3	50.95	17.85	-15.69	0.244	-1.032	-0.335	H
SDSSJ131217.40+125206.5	54.14	16.15	-17.51	0.391	-1.009	-0.489	H

TABLE 4.4 – *Continued*

Galaxy Name (1)	D (Mpc) (2)	m_g (3)	M_g (4)	$\log[\text{OIII}]/\text{H}\beta$ (5)	$\log[\text{NII}]/\text{H}\alpha$ (6)	$\log[\text{SII}]/\text{H}\alpha$ (7)	Classification (8)
SDSSJ131258.35+122840.7	53.45	16.38	-17.26	0.503	-1.081	-0.768	H
SDSSJ131300.25+123648.9	53.51	17.49	-16.15	0.707	-1.376	-0.891	H
SDSSJ131343.75+124616.8	55.96	16.86	-16.88	0.231	-1.249	-0.156	H
SDSSJ131623.94+123120.1	55.37	17.91	-15.81	0.490	-1.184	-0.534	H
SDSSJ131635.77+120908.6	54.49	17.14	-16.54	0.560	-1.097	-0.613	H
SDSSJ131652.31+123253.6	14.41	14.47	-16.32	0.295	-0.943	-0.544	H
SDSSJ132733.57+114348.6	66.60	17.29	-16.83	0.279	-0.913	-0.219	H
SDSSJ132852.21+110549.2	67.43	16.03	-18.12	0.373	-0.926	-0.521	H
SDSSJ133156.93+133101.6	75.16	17.95	-16.43	0.746	-1.443	-0.984	H
SDSSJ133812.60+155147.5	71.25	17.15	-17.12	0.214	-0.983	-0.355	H
SDSSJ134201.80+144233.7	71.92	17.53	-16.76	0.534	-1.579	-0.769	H
SDSSJ134522.56+112210.9	76.57	17.85	-16.57	0.580	-1.657	-0.918	H

NOTES—Col. (1): Galaxy name from SDSS. Col. (2): Distance, in Mpc, as calculated in Sec. 3.1. Col. (3): Apparent g -magnitude, from SDSS. Col. (4): Absolute g -Magnitude, as calculated in Eqn. 3.5. Cols. (5)–(7): Line-Intensity ratios; [SII] is the sum of the [SII] $\lambda\lambda$ 6716, 6731 doublet. Col. (8): Classification of nuclear spectrum, as described in Sec. 4.5: H = HII nucleus, S = Seyfert Galaxy, L = LINER, E = Early-type galaxy.

4.6 Completeness of SDSS

One other important result that we have gleaned from this pilot study is the relative usefulness of SDSS as a way to find AGNs. Of the 316 galaxies in our sample, only 200 can be spectrally classified as AGN or non-AGN based on their SDSS spectra alone (“classifiable” galaxies). “Non-classifiable galaxies” either do not have a nuclear spectrum in SDSS, or have a nuclear spectrum that is too noisy to permit spectral classification of the galaxy. Based on this data, we see that SDSS is only 63% complete out to 80 Mpc.

Moreover, the SDSS completeness does not significantly improve by imposing a smaller distance limit. The relationship between luminosity, distance and the completeness of SDSS is demonstrated in Figures 4.10 and 4.11. Figure 4.10 demonstrates the absolute magnitude distribution of the galaxies for which SDSS has spectra, compared to the galaxies for which SDSS spectroscopic data is incomplete. It is clear that SDSS spectroscopic coverage decreases greatly for faint galaxies. Moreover, Figure 4.11 demonstrates that the completeness does not depend on distance, so completeness cannot be improved by imposing a closer distance limit. This analysis makes it clear that it is crucial to include other resources when compiling a complete sample of galaxies, and demonstrates the necessity of follow-up observations.

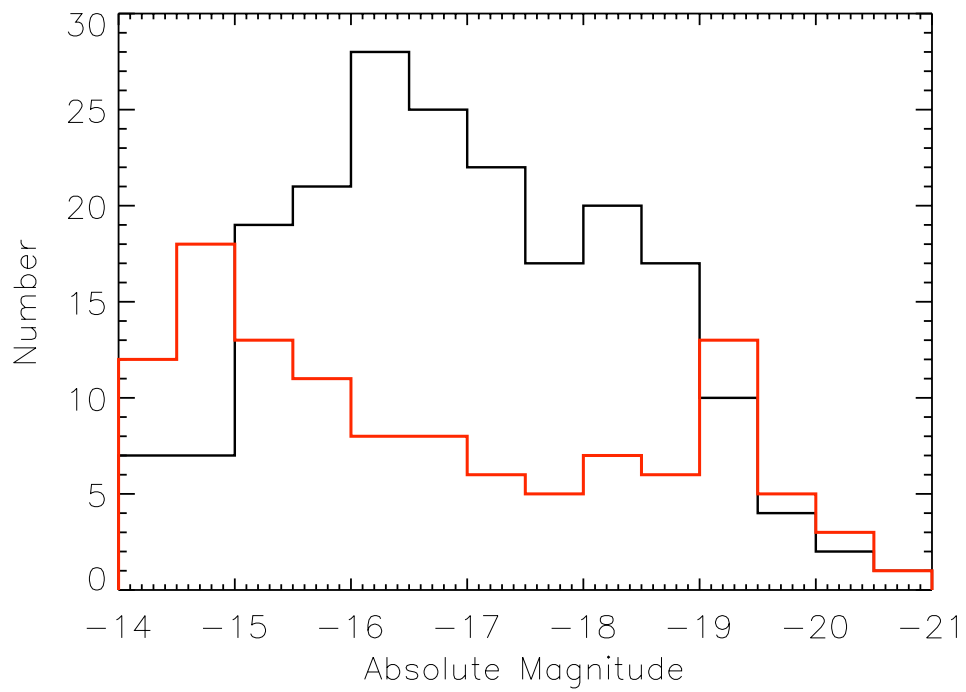


Figure 4.10: The absolute magnitude distribution of galaxies for the galaxies that are classifiable from SDSS spectra (black line) and not classifiable (red line). There is a sharp drop in SDSS completeness fainter than $M_g = -15$. The spike at -19 reflects the fact that SDSS does not obtain nuclear spectra of very bright galaxies because the spectra would saturate.

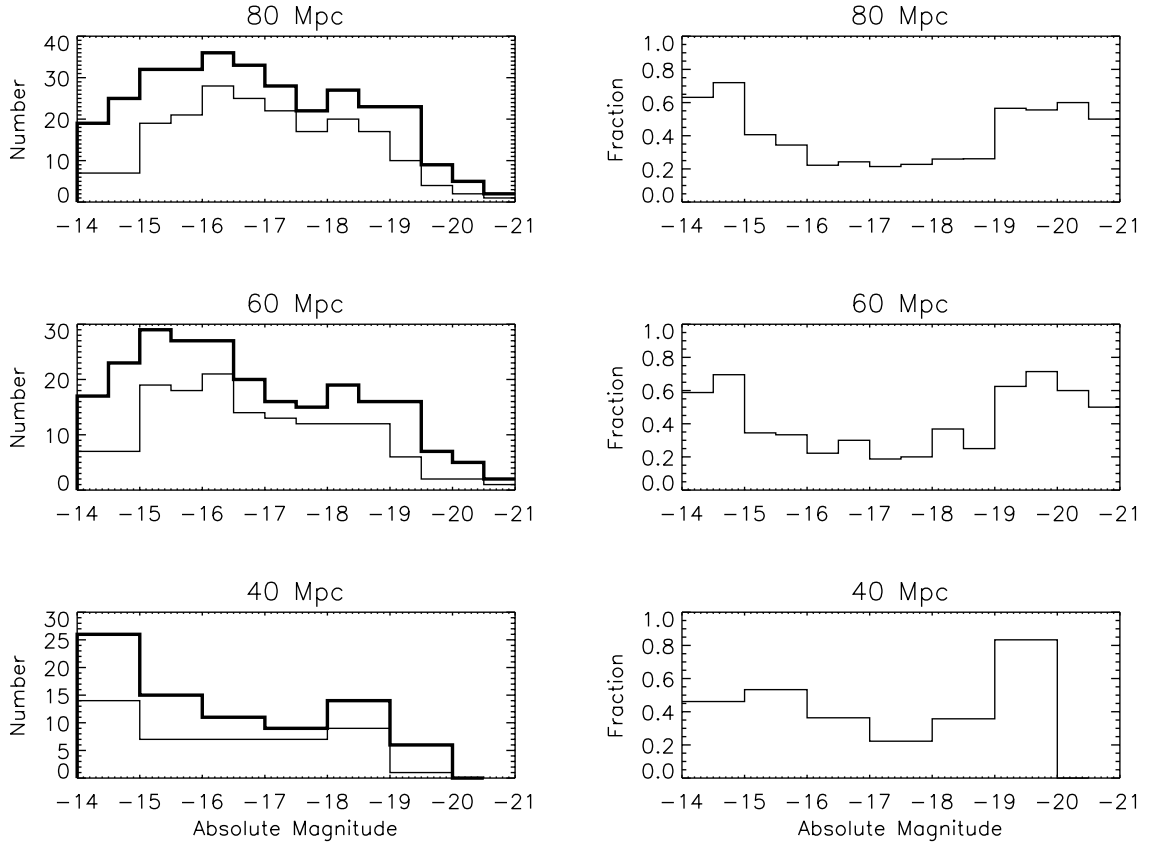


Figure 4.11: The completeness of SDSS as a function of distance and magnitude. The graphs on the left compare total number of objects in our sample (thick line) to number of galaxies for which SDSS has a classifiable spectra (thin line) out to 80 Mpc, 60 Mpc, and 40 Mpc. The graphs on the right provide an indication of the fractional completeness of SDSS as a function of magnitude at the three distance limits (taller bins equate to less completeness). Width of each bin corresponds to 0.5 mag (top two graphs) and 1 mag (bottom graph, where the noise created by the small numbers involved would overwhelm the significance of the data with smaller bins).

Chapter 5

Summary and Conclusions

The purpose of this research has been to probe the properties of supermassive black holes and their host galaxies by extending the number of known AGNs into the low-host galaxy luminosity and low-bulge luminosity region. The results from our study demonstrate that putting together a volume-limited sample allows for many more low-luminosity (and therefore low-mass) galaxies to be found, increasing the likelihood of finding intermediate mass black holes. Indeed, by using a volume-limited approach, we have found a population of AGNs that have characteristically different properties than the general population of known active galactic nuclei.

The success of our sample population is best demonstrated by its relationship to results from other approaches to extragalactic surveys. As we have seen, in our area of the sky, we have found more than 16 times the number of galaxies as the “gold-standard” HFS survey for low-luminosity AGNs found in the same region. Additionally, our survey has been exceptionally successful at finding many galaxies in the low-luminosity range, which is virtually unexplored in the context of AGN research. Moreover, we have accomplished this feat using publicly available resources, demonstrating that this is an easy way to conduct such a survey, and an efficient use of existing data.

Of course, the most exciting results from this study are the AGNs that we

have found. There are 17 AGNs in our region, 12 of which have never before been classified as AGNs, and none of which have been extensively studied. Six of these AGN are definite Seyfert Galaxies, none of which were previously known to exist in our survey volume. This demonstrates the effectiveness of our approach to finding AGNs, especially considering that our region covers a mere $\sim 0.6\%$ of the sky, and only extends to a distance of 80 Mpc.

With such remarkable results, the future of volume-limited AGN surveys looks bright. There is much work left to be done, both with this sample and in extending the sample to a larger region of the sky. For our sample, we wish to continue obtaining follow up spectra to increase the overall completeness. Additionally, we hope to acquire additional data that will allow us to begin directly studying the properties of the black holes. Meanwhile, we are ready to extend the procedures developed by this project to a larger region of space. As discussed in Chapter 2, the eventual area of overlap between SDSS and ALFALFA will cover ~ 4800 deg², roughly 20 times the area of our pilot study. An initial exploration of what SDSS has to offer over a larger area of the sky has already begun, and results look promising. The door is now open to a multitude of future prospects in intermediate mass black hole research.

Appendix A

Distance Calculations

The following is a walk-through of how to execute distance corrections for a galaxy, knowing its RA, Dec, heliocentric velocity, and galactic coordinates (l, b).

Start by defining physical constants:

Cluster	RA	Dec	V_H	V_{LG}	V_{fid}
Virgo	187.711	12.390	1035	957	200
Great Attractor	200.547	-43.737	4600	4380	400

Hubble's constant:
 $H_0 = 73$

Calculate the angle between the galaxy and the Virgo Cluster:

$$\begin{aligned}x &= \sin(\text{RA}_{\text{Virgo}}) \times \cos(\text{Dec}_{\text{Virgo}}) \times \sin(\text{RA}) \times \cos(\text{Dec}) \\y &= \cos(\text{RA}_{\text{Virgo}}) \times \cos(\text{Dec}_{\text{Virgo}}) \times \cos(\text{RA}) \times \cos(\text{Dec}) \\z &= \sin(\text{Dec}_{\text{Virgo}}) \times \sin(\text{Dec}) \\\cos \theta_V &= x + y + z\end{aligned}$$

Take into account the galaxies in the Virgo cluster, using a radius of 10 degrees around the center coordinates of the cluster and a velocity range of 600-2300 km/s:

if $(\arccos(\cos \theta_V)) < 10$ and $(V_H > 600)$ and $(V_H < 2300)$ do:
 Distance = 13.9 Mpc

For all non-virgo galaxies, calculate the cosine of the angle between the galaxy and the Great Attractor:

$$\begin{aligned}
x_{GA} &= \sin(RA_{GA}) \times \cos(Dec_{GA}) \times \sin(RA) \times \cos(Dec) \\
y_{GA} &= \cos(RA_{GA}) \times \cos(Dec_{GA}) \times \cos(RA) \times \cos(Dec) \\
z_{GA} &= \sin(Dec_{GA}) \times \sin(Dec) \\
\cos \theta_{GA} &= x_{GA} + y_{GA} + z_{GA}
\end{aligned}$$

Correct for Local group infall, from Karachentsev and Makarov (1996),
using the coordinates (93,-4) for the direction of the sun's motion
with respect to the local group (equation 3.1):

$$V_0 = V_H + 316(\cos(b) \cos(-4) \cos(l - (93)) + \sin(b) \sin(-4))$$

Calculate r_v , the estimated distance between the object from virgo,
expressed as a velocity:

$$r_v = \sqrt{V_0^2 + V_{LG}^2 - 2V_0V_{LG} \cos \theta_V}$$

Calculate V_{Virgo} , the correction for infall into the Virgo cluster:

$$\begin{aligned}
V_{Virgo} &= V_{fidVirgo} \cos \theta_V + V_{fidVirgo} \left(\frac{V_0 - V_{LG} \cos \theta_V}{r_v} \right) \left(\frac{V_{LG}}{r_v} \right) \\
V_{new} &= V_{Virgo} + V_0
\end{aligned}$$

Calculate r_{GA} , the estimated distance between the object from the
great attractor, expressed as a velocity:

$$r_{GA} = \sqrt{V_{new}^2 + V_{LG,GA}^2 - 2V_{new}V_{LG,GA} \cos \theta_{GA}}$$

Calculate V_{GA} , the correction for infall into the Great Attractor

$$V_{GA} = V_{fid,GA} \cos \theta_{GA} + V_{fid,GA} \left(\frac{V_{new} - V_{LG,GA} \cos \theta_{GA}}{r_{GA}} \right) \left(\frac{V_{LG,GA}}{r_{GA}} \right)$$

Calculate V_{cosmic} , the final corrected velocity:

$$V_{cosmic} = V_0 + V_{Virgo} + V_{GA}$$

Apply Hubble's Law:

$$\text{Distance} = V_{cosmic} / H_0$$

Appendix B

Spectral Absorption and Emission

Spectroscopy is one of the most powerful tools that modern astronomy has at its disposal, because “signatures” of different elements can be seen in starlight, allowing us to discern, among other things, the chemical composition of stars. Some essential background about spectroscopy is discussed here.

A Brief History of Spectroscopy

In the early 19th century, scientists began seriously studying what happens when light is shined through a prism. Of course, it was well known that sunlight shining through a prism will produce rainbows, but nobody had investigated the phenomenon much further than that. William Wollaston (1766-1828) was the first to notice that a number of dark lines could be discerned within the continuous spectrum of the sun’s light. A few years later, Joseph von Fraunhofer had begun to catalogue those dark **absorption lines**. As he catalogued these lines, he noticed that one particularly prominent line occurred at the same yellow wavelength as the color of the light emitted when salt is sprinkled on a candle flame (Carroll & Ostlie 2007). This kicked off the science of spectroscopy, and it didn’t take long for other scientists to start burning elements and cataloguing each element’s characteristic wavelength signature. For instance, Gustav Kirchhoff (1824-1887) was able to match 70 absorption lines in the solar spectrum to 70 bright **emission lines** that are produced by iron vapor (Carroll & Ostlie 2007). Kirchhoff also summarized his observations of the production of spectral features in three concise laws:

- Hot, dense gases or hot solid objects produce continuous spectra (rainbows) with no absorption lines:



- Hot, diffuse gas produces emission lines on an otherwise dark spectrum:



- Cool, diffuse gas in front of a source of a continuum spectra, you get absorption lines “interrupting” the otherwise continuous spectra:



Physical Explanation

At this point, 18th century scientists knew that if pure white light shines through a cool gas, some of the light is absorbed. This absorption occurs at specific wavelengths which depend on the chemical composition of the gas. If you heat up that same gas, it will produce bright emission lines at the same wavelengths where it was previously absorbing. What could be causing these phenomena?

Niels Bohr was the first to offer an explanation of why gases act in these odd ways. He proposed a new model of the atom, the **Bohr Model** or **Semiclassical Model** of the atom. In this model, electrons orbit around the nucleus of the atom (made of protons and neutrons) in much the same way as the moon orbits around the earth. These electrons are free to “jump” to higher-energy orbital states if something comes along that gives them the extra energy to do so. However, an electron is not free to orbit at any energy it chooses, but is confined to specific orbital levels. In other words, the orbital levels form a ladder, not a ramp.

How does this model of the atom account for absorption lines? Suppose a photon from a star is traveling through space, and encounters an atom. If it has precisely the same energy as one of the orbital “steps”, it can impart that energy to the electron, which transfers to a higher energy state, and the photon is (temporarily) lost. What we see in this case conforms to Kirchoff’s third law, where the background light would shine through the gas, except where the light has just the right amount of energy to excite the gas molecules.

The Bohr model is also all we need to explain emission lines and Kirchoff’s second law. If a gas is very hot (or has a lot of energy from some other source), the electrons have enough energy to spontaneously and frequently jump to higher states. They will also spontaneously “fall” back down to lower energy states, but they have to release the energy they were holding in order to do so. This energy is released in the form of a photon with precisely enough energy to “drop” the electron back down to its lower state. Figure B.1 demonstrates both absorption and emission in the Bohr model of the atom.

Because every element has electron orbitals corresponding to different energy levels, and therefore different wavelengths, observing emission and absorption lines gives astronomers essential knowledge about what elements are present in different regions of space. Without spectroscopy, many of the most important astronomical discoveries of our time would not have been possible.

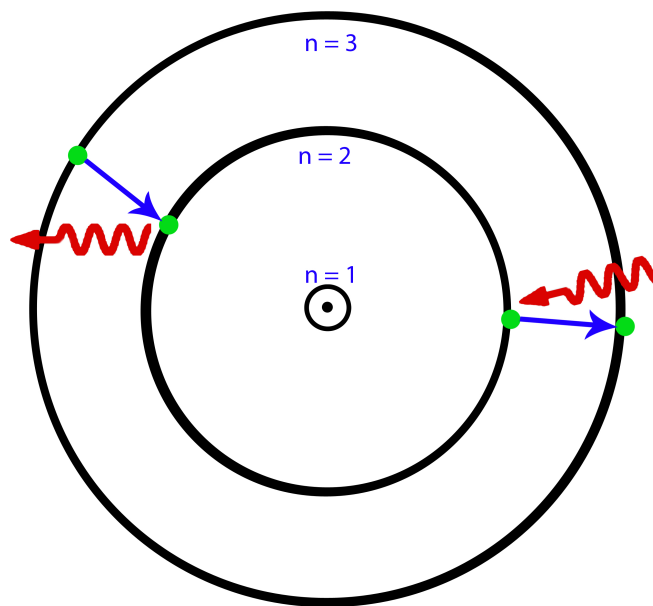


Figure B.1: The Bohr Atom. On the left, an electron (green dot) is “falling” from the 3^{rd} energy state to the 2^{nd} , and emitting a photon. On the right, an electron is getting excited by an incoming photon and “jumping” to a higher energy state.

Appendix C

The Nature of LINERs

While some fraction of observed Low-Ionization Emission-Line Regions (LINERs) have definitive evidence that a central black hole is causing the emission line spectra, in other LINER galaxies it is not as clear, and it is possible that other excitation processes are involved. If black holes are not the energy source in LINERs, possible alternative engines include stellar photoionization (Shields 1992) and shock heating (Terlevich et al. 1992). However, if black holes are indeed the energy source in LINERs, there must be some physical difference that distinguishes LINERs from Seyfert galaxies.

The Viability of Supernova or O-star Excitation

One of the early options that was proposed as the excitation mechanism for LINERs was stellar photoionization. While ordinary O-type stars with effective temperatures typical of those found in HII regions in galactic disks do not produce enough low-energy ionization lines to produce a LINER-like spectrum, the conditions in the center regions of galaxies may be more conducive to producing LINER spectra with O-stars as the ionizing source (Ho 2008). However, studies of the stellar populations in the nuclei of LINERs indicate that this is improbable.

Fernandes et al. (2004) and HFS (2003) conducted spectroscopic studies of the stellar populations of LINERs to investigate whether hot stars are a realistic ionizing source in these galaxies. One very significant result of their observations is that the Wolf-Rayet spectral bump centered at 4640\AA , which is the clear signature of a young stellar population, was not observed in any of the LINERs in the study. In other words, starbursts younger than 10^7 years did not contribute a significant fraction of light to

any of the LINERs observed (Fernandes et al 2004; HFS 2003). The lack of young stars in the LINERs observed in this study rules out the possibility that either O-star emission or supernova excitation is responsible for LINER spectra, unless counter-examples of star-forming LINERs are found in further studies.

Photoionization by Post-AGB Stars

In addition to O-star photoionization, photoionization by intermediate-mass stars has also been proposed. Taniguchi et al. (2000) proposed that in galaxies which have previously gone through a starburst phase, post-asymptotic giant branch (AGB) intermediate-mass (several M_{\odot}) stars could be causing LINER emission through the photoionization of interstellar gas. Their starburst models indicated that after stars went through the AGB phase, each star would lose its gaseous envelope, creating a planetary nebula and leaving behind a hot core. These planetary nebula nuclei (PNNs) could potentially be very hot ($T_{\text{eff}} > 10^5$ K), and thus capable of being a major photoionization source. However, this model is limited to LINERs in late-type (post-S0) galaxies, where the galaxies are likely to have undergone a starburst period within the last $\sim 10^8$ years. Therefore, another explanation is necessary to account for LINERs in elliptical galaxies.

Shock Excitation

Another theory that has been a popular contender as a method for excitation in LINERs is collisional ionization by shocks. Dopita & Sutherland (1995) model fast shocks propagating through the interstellar medium and examine the emission-line ratios that are produced by the models. The models were moderately successful at matching emission-line ratios that are observed, so it is possible that shocks could play a significant role in LINER emission.

If shocks contribute to the excitation that is seen in LINERs, it is important to understand what is driving the shocks in the first place. The most viable options are

accretion-driven or jet-driven shocks. Both of these options involve a central object that is accreting matter, so they are not necessarily incompatible with a black-hole hypothesis. Indeed, it is almost certain that shocks are present in some way in AGNs, the unknown factor is the balance between the relative strengths of the effects caused by shocks and photoionization (Ho 2008).

The significance that shock-excitation has in producing LINER-type spectra is still uncertain. Accretion- or jet-driven shocks are not at odds with the black hole model for AGNs, and wherever there is a significant amount of gas accreting onto an object, some degree of shock-heating will occur (Ho 2008). The issue is how much shocks contribute to the overall excitation budget of LINERs. Ho (2008) argues that recent evidence demonstrates that fast-shocks are unlikely to be common in LINERs. First, the UV spectra of LINERs are inconsistent with the fast-shock models because high-energy excitation lines (such as C IV $\lambda 1549$ and He II $\lambda 1640$) have not been observed at the intensities predicted by shock-heating. Additionally, evidence from the HFS survey of low-luminosity AGNs does not show evidence for the high velocity dispersions that are required for the fast-shock excitation scenario (Filippenko 2003; Ho 2008; HFS 2003). Therefore, while shocks may be present in LINERs, they are unlikely to be the main cause of the observed emission lines.

LINERs as true AGNs: The Black Hole Hypothesis

There is increasing evidence that many (if not all) LINERs are powered by accretion around a supermassive black hole. Several different observational characteristics can indicate the presence of a black hole in a LINER. Observing a compact X-ray or radio core at the center of a galaxy is one clear indication, while the detection of broad-line regions also provides evidence in favor of black holes (Filippenko 2003; Ho 2008). In the case that LINERs are powered by accretion, the physical mechanism that distinguishes LINERs from Seyferts must be discussed.

In LINER galaxies where compact radio or X-ray cores are detected, it is safe to assume that a black hole is present in the galaxy. Radio cores have been successfully discovered in 64% of the LINERs in the HFS sample. These cores appear to be non-stellar in nature, and have brightness temperatures $T > 10^7$ K (Ho 2008). Additionally, compact X-ray cores have been discovered in about 75% of LINERs and TOs in the HFS survey, suggesting that most of these objects do contain AGNs, although further statistical analysis is necessary (Filippenko 2003; Ho 2008). In either case, a compact core is strong evidence for accretion around a black hole.

Detection of broad-line emission of permitted lines is often assumed to be a clear indication of a true AGN (Ho 2008; Filippenko 2003). Therefore, many consider all LINERs with detectable broad lines (LINER 1s) or LINER 2s with a detectable hidden broad line region to be AGNs (Ho 1999; Ho 2008; Filippenko 2003). Filippenko (2003) found that 24% of LINER galaxies in the HFS survey had detectable broad-line emission, although it is possible that additional LINER 1s were not detected because the broad component was below the sensitivity limit of the observations.

In those cases where there is compelling evidence for black hole accretion as the “engine” in LINERs, there must be some physical difference that makes their spectra much lower-energy than seen in Seyfert galaxies. One possibility is that there is simply less matter accreting onto the black hole. This would imply that LINERs exist in comparatively gas-poor galaxies. However, Ho (2008) points out that there is very little gas required to “light-up” an AGN. This fact, combined with the amounts of gas lost by stars during the normal course of evolution, and observations of gas abundances and temperatures in the cores of elliptical galaxies indicate that there is plenty of fuel for an AGN even in the most gas-poor environments (Ho 2008). Therefore, there must be another influence on the LINER spectra that distinguish them from Seyferts.

If there is plenty of fuel for LINERs, there must be something that is slowing the radiation that the accretion would otherwise be causing. If the material that is accreting

onto the black hole is so tenuous that its cooling time is longer than the time it takes to fully accrete, the accretion will be radiatively inefficient (Ho 2008). If the energy from the gas cannot radiate, it must be released in some other form, either through convective transport or through an outflowing wind. Either process would decrease the accretion rate significantly, and cause the lower energies that are evident in LINER spectra. Inefficient accretion models have been successfully applied to LINERs by Chiaberge & Macchetto (2006), Nemmen et al. (2006), and others. More advanced modeling and detailed observations are needed to determine the exact cause of the energy signature of LINER galaxies.

For now, it is safe to assume that many LINERs are primarily powered by accretion onto a central black hole. However, photoionization by shock-heating or post-AGB stars may play a role, either independently or alongside black hole excitation, and these possibilities are worthy of further investigation.

Bibliography

- Abazajian, K., et al. 2008, ArXiv e-prints
- Baldwin, J. A., Phillips, M. M., & Terlevich, R. 1981, PASP, 93, 5
- Barth, A. J., Greene, J. E., & Ho, L. C. 2005, ApJ, 619, L151
- . 2008, AJ, 136, 1179
- Barth, A. J., Ho, L. C., Rutledge, R. E., & Sargent, W. L. W. 2004, ApJ, 607, 90
- Bell, E. F. 2003, ApJ, 586, 794
- Bentz, M. C., Peterson, B. M., Pogge, R. W., & Vestergaard, M. 2009, ApJ, 694, L166
- Blanton, M. R., et al. 2001, AJ, 121, 2358
- Bombaci, I. 1996, AA, 305, 871
- Carroll, B. W., & Ostlie, D. A. 2007, An Introduction to Modern Astrophysics, ed. B. W. Carroll & D. A. Ostlie (Pearson, Addison, Wesley)
- Chiaberge, M., & Macchetto, D. 2006, in Bulletin of the American Astronomical Society, Vol. 38, Bulletin of the American Astronomical Society, 988
- Dieck, C. 2008, Master's thesis, Wesleyan University
- Dopita, M. A., & Sutherland, R. S. 1995, ApJ, 455, 468
- Fernandes, R. C., et al. 2004, ApJ, 605, 105
- Filippenko, A. V. 2003, in ASPCS, Vol. 290, Active Galactic Nuclei: From Central Engine to Host Galaxy, ed. S. Collin, F. Combes, & I. Shlosman, 369

- Filippenko, A. V., & Sargent, W. L. W. 1985, *ApJS*, 57, 503
- Gebhardt, K., et al. 2000, *ApJ*, 539, L13
- Ghez, A. M., Salim, S., Hornstein, S. D., Tanner, A., Lu, J. R., Morris, M., Becklin, E. E., & Duchêne, G. 2005, *ApJ*, 620, 744
- Giovanelli, R., et al. 2005, *AJ*, 130, 2598
- . 2007, *AJ*, 133, 2569
- Greene, J. E., Barth, A. J., & Ho, L. C. 2006, *New Astronomy Review*, 50, 739
- Greene, J. E., & Ho, L. C. 2007a, *ApJ*, 670, 92
- . 2007b, *ApJ*, 667, 131
- Ho, L. C. 2008, *ARA&A*, 46, 475
- Ho, L. C., Filippenko, A. V., & Sargent, W. L. 1995, *ApJS*, 98, 477
- Ho, L. C., Filippenko, A. V., & Sargent, W. L. W. 1997a, *ApJS*, 112, 315
- . 1997b, *ApJS*, 487, 568
- . 2003, *ApJ*, 583, 159
- Ho, L. C., Filippenko, A. V., Sargent, W. L. W., & Peng, C. Y. 1997c, *ApJS*, 112, 391
- Karachentsev, I. D., & Makarov, D. A. 1996, *AJ*, 111, 794
- Kauffmann, G., et al. 2003, *MNRAS*, 346, 1055
- Kewley, L. J., Groves, B., Kauffmann, G., & Heckman, T. 2006, *MNRAS*, 372, 961
- King, A. 2003, *ApJ*, 596, L27
- Kormendy, J., & Richstone, D. 1995, *ARA&A*, 33, 581

- Laor, A. 2007, in *Astronomical Society of the Pacific Conference Series*, Vol. 373, *The Central Engine of Active Galactic Nuclei*, ed. L. C. Ho & J.-W. Wang, 384
- Marconi, A., & Hunt, L. K. 2003, *ApJ*, 589, L21
- Mould, J. R., et al. 2000, *ApJ*, 529, 786
- Nemmen, R. S., Storchi-Bergmann, T., Yuan, F., Eracleous, M., Terashima, Y., & Wilson, A. S. 2006, *ApJ*, 643, 652
- Osterbrock, D. E., & Ferland, G. J. 2006, *Astrophysics of Gaseous Nebulae and Active Galactic Nuclei*, ed. D. E. Osterbrock & G. J. Ferland (University Science Books, 2006)
- Peterson, B. M., et al. 2005, *ApJ*, 632, 799
- Prestwich, A. H., et al. 2007, *ApJ*, 669, L21
- Robertson, B., Hernquist, L., Cox, T. J., Di Matteo, T., Hopkins, P. F., Martini, P., & Springel, V. 2006, *ApJ*, 641, 90
- Seyfert, C. K. 1943, *ApJ*, 97, 28
- Shields, J. C. 1992, *ApJ*, 399, L27
- Taniguchi, Y., Shioya, Y., & Murayama, T. 2000, *AJ*, 120, 1265
- Terlevich, R., Tenorio-Tagle, G., Franco, J., & Melnick, J. 1992, *MNRAS*, 255, 713
- Tremaine, S., et al. 2002, *ApJ*, 574, 740
- Veilleux, S., & Osterbrock, D. E. 1987, *ApJS*, 63, 295
- Volonteri, M., Lodato, G., & Natarajan, P. 2008, *MNRAS*, 383, 1079
- Yasuda, N., et al. 2001, *AJ*, 122, 1104

York, D. G., et al. 2000, AJ, 120, 1579